

**SYNTHESIS OF ARTIFICIAL METAL (Fe, Mg)  
SILICATE DEPOSITS UNDER HIGH PRESSURE AND  
TEMPERATURE CONDITIONS AND DEVELOPMENT  
OF POLYMERIC INHIBITOR FOR METAL SILICATE  
SCALING**

A Thesis Submitted to  
the Graduate School of Engineering and Sciences of  
Izmir Institute of Technology  
in Partial Fulfillment of the Requirements for the Degree of  
**MASTER OF SCIENCE**  
in Materials Science and Engineering

by  
Ashlı ÇELİK

**July 2017**  
**İZMİR**

We approve the thesis of **Aslı ÇELİK**

**Examining Committee Members:**

---

**Prof. Dr. Mustafa M. DEMİR**

Department of Materials Science and Engineering, Izmir Institute of Technology

---

**Prof. Dr. Alper BABA**

Department of Civil Engineering, Izmir Institute of Technology

---

**Prof. Dr. Gültekin TARCAN**

Department of Geological Engineering, Dokuz Eylül University

**24 July 2017**

---

**Prof. Dr. Mustafa M. DEMİR**

Supervisor, Department of Materials Science and Engineering,  
İzmir Institute of Technology

---

**Prof. Dr. Mustafa M. DEMİR**

Head of the Department of Materials  
Science and Engineering

---

**Prof. Dr. Aysun SOFUOĞLU**

Dean of the Graduate School of  
Engineering and Sciences

## ACKNOWLEDGEMENTS

There are number of people that I owe to thank to finish my master thesis with the help of their patience, guidance, emotional support and understanding.

To my supervisor, Prof. Dr. Mustafa M. DEMİR, for his full support, excellent guidance, supply of a great working area and research opportunity and encouragement for the last three years. I can't imagine finishing this thesis without his extensive knowledge and endless help.

Beside my advisor, I would like to thank to my co-advisor Prof. Dr. Ahmet E. EROĞLU, Assoc. Prof. Dr. Yasar AKDOGAN and Assist. Prof. Dr. Ufuk ŞENTÜRK for their guidance and aid, and rest of my thesis committee: Prof. Dr. Alper BABA and Prof. Dr. Gültekin TARCAN.

To members of Demir Research Lab, Anıl İNCEL, Tuğba ISIK, Tuğrul GÜNER for their help, great patience and understandings and specifically to my co-worker Gökhan TOPÇU for his support at synthesis of polymers part and rest of my study.

Special thanks to The Scientific and Technological Research Council of Turkey (TUBITAK) with a project number 14Z940 for the foundation of this research.

To TUZLA JES A.Ş. and Gonca KOÇ for their sample and information support and their friendliness.

To my friends at İYTE, Nilüfer HOŞBAHTLI, İffet AKKUŞ, Merve AKBAL, Ayten Ekin MEŞE, Müge YÜCEL, Gün Deniz AKKOÇ, İpek HARMANLI, Başak BAŞAR and Esra CİHAN for their emotional support and being with me all the time.

I am as well express my appreciations for their patience, aid and friendliness to Environmental Development Application and Research Center specialist Sanem Ezgi KINAL and Ege University Center Laboratory EGE MATAL specialist Aysegül ERDOGAN.

Finally, my sincere thanks to my family, Canan, Mustafa and Emre Cem ÇELİK, and my love Birol BERBER for supporting me spiritually throughout my entire study and encourage my activities.

## **ABSTRACT**

### **SYNTHESIS OF ARTIFICIAL METAL (Fe, Mg) SILICATE DEPOSITS UNDER HIGH PRESSURE AND TEMPERATURE CONDITIONS AND DEVELOPMENT OF POLYMERIC INHIBITOR FOR METAL SILICATE SCALING**

Turkey has to import energy from other countries, because of having not enough sources. Geothermal energy is one of the renewable energy that can be readily founded in Turkey. At the core of the Earth by definition, the high temperature and pressure cause some rock to melt, creating magma convection upward since it is lighter than the solid rock. The magma heats rock and water in the crust.

Tuzla geothermal field is the study area and there are NaCl, Mg ,Fe,Si , Ca and Zn metals and CO<sub>2</sub> (g) in brine. While geothermal fluids are pumped from down to top the temperature and pressure decreased and CO<sub>2</sub> is released. So, the pH level increases and causes silicate, sulfonate and calcide scaling problems. Moreover, silica is reacted with metal oxides to more stable scales. The production of electricity decreases and while cleaning and the system is shot-down. The present method of strong acid cleaning, harms components as well as create potential risk for the health of employees.

In this project, artificial metal-silicate deposit was synthesized with close composition and morphology to natural scale, and potential inhibitors were synthesized and tested. Firstly, synthesizing of artificial deposit is necessary in the laboratory setting. For this purpose, we can simulate the course of temperature and pressure values will be used in autoclave reactor system. Secondly, the functional groups that exhibit inhibitory feature(s) have the potential of macromolecules (Poly (vinyl sulfonic acid), Poly (vinyl phophonic acid), Polyacrylamide and their copolymers and tercopolymer) were tested.

## ÖZET

# YÜKSEK SICAKLIK VE BASINÇ ALTINDA YAPAY METAL (Fe, Mg) SİLİKAT ELDESİ VE METAL SİLİKAT KABUKLAŞMASINA YÖNELİK POLİMERİK İNHİBİTÖR GELİŞTİRİLMESİ

Son yıllarda artan enerji talebi ile birlikte Türkiye fosil yakıtlara bağımlılığı sebebiyle bir enerji darboğazından geçmektedir. Enerji taleplerinin karşılanamaması sebebiyle de dışa bağımlı durumdadır. Hem enerji konusundaki dışa bağımlılığından kurtulmak hem de enerji ihtiyacını karşılamak için Türkiye alternatif enerji kaynaklarına yönelmektedir. Jeotermal enerji, yeraltı sularının magmaya yakın ısıtıcı kayaçlardan alarak yerkabığında depolanan enerjinin elektrik enerjisine dönüştürülebildiği döngüsel ve sürdürülebilir bir enerji türüdür.

Kabuklaşmanın görüldüğü jeotermal saha Tuzla jeotermal sahasıdır ve kuyu suyunun yapısında NaCl tuzu ile, Mg, Ca, Fe, Si ve Zn iyonlarının yanı sıra yüksek oranda çözünmüş CO<sub>2</sub> gazı bulunmaktadır. Enerji üretimi esnasında yeraltında yerüstüne çıkarılan suyun sıcaklığı düşmektedir. Sıcaklık ve basınç düşüşü ile birlikte karbondioksit gazı sistemde sıvıdan buhar fazına geçmekte ve pH seviyesi bazlığa doğru kaymaktadır. Bu durum kalsit, silikat, sülfat vb.... gibi kabuklaşma oluşumuna sebep olmaktadır. Asitliğin düşmesi ile birlikte oluşan metallerin oksit formları da oluşan silikat yapısına katılarak daha da giderimi zor bir hale getirmektedir. Silikat kabuklaşması sebebiyle jeotermal sistemin bileşenleri daralıp tıkanmakta ve çözüm olarak gerçekleştirilen kuvvetli asit ile mekanik temizlik işlemi sebebiyle hem üretim verimi düşmekte hem de sistem zarar görmektedir.

Bu projede, doğal kabuğa en yakın morfoloji ve kompozisyondaki yapay kabuk sentezlenmiş, potansiyel inhibitörler dizayn edilmiş, sentezlenmiş ve test edilmiştir. İlk aşamada jeotermal sahanın koşullarını simüle edebildiğimiz otoklav reaktör sistemi ile sentetik kabuk sentezi gerçekleştirilmiştir. İkinci aşamada ise, potansiyel inhibitör olabilecek makromoleküllerin (Poli (vinil sülfonik asit), Poli (vinil fosfonik asit), Poliakrilamat ile bu moleküllerin kopolimerleri ve terkopolimeri) inhibitör performansları test edilmiştir.

*Dedicated to my family...*

## TABLE OF CONTENTS

LIST OF FIGURES .....	ix
LIST OF TABLES.....	xi
CHAPTER 1. INTRODUCTION .....	1
1.1. Geothermal Energy and Scaling Problem.....	1
1.2. Types of Scaling .....	2
1.3. Literature Review.....	3
1.3.1. Mechanism of Scaling .....	3
1.3.2. Inhibitor Chemistry .....	5
1.4. Aim of the Study.....	10
CHAPTER 2.EXPERIMENTAL .....	12
2.1. Materials and Methods.....	12
2.2. Synthesis of Artificial Metal Silicate Deposits.....	13
2.2.1 Effect of Metal Cations .....	15
2.3. Characterization of Brine and Decantate .....	15
2.4. Characterizations of Natural Scale and Artificial Deposits .....	16
2.5. Synthesis of Polymers.....	16
2.6. Characterization of Polymers.....	17
2.7. Inhibitor Tests .....	17
2.8. Characterization Tools .....	18
2.8.1. Inductively Coupled Plasma-Mass Spectrometry (ICP-MS) .....	18
2.8.2. Ion Chromatography (IC) .....	18
2.8.3. UV-Silicomolybdate Spectrophotometry .....	19
2.8.4. X-Ray Diffractometer (XRD).....	19
2.8.5. X-Ray Fluorescence (XRF) .....	19
2.8.6. Scanning Electron Microscope (SEM).....	20
2.8.7. X-Ray Photoelectron Spectrometry (XPS).....	20
2.8.8. Electron Paramagnetic Resonance Spectrometer (EPR) .....	20

2.8.9. Nuclear Magnetic Resonance (NMR) .....	21
2.8.10. Dynamic Light Scattering (DLS) .....	21
2.8.11. Fourier Transform Infrared Spectrometer (FTIR) .....	21
 CHAPTER 3.RESULTS AND DISCUSSION.....	22
3.1. Hydrogeochemical Properties of Geothermal Fluids.....	22
3.2. Morphology and Structure of the Deposits .....	24
3.3. Spectroscopic Characterization of the Deposits .....	26
3.4. Effect of Metal Cations .....	31
3.5. Inhibition of Scale by Polymeric Compounds .....	32
 CHAPTER 4.CONCLUSION .....	40
 REFERENCES .....	42

## LIST OF FIGURES

<u>Figure</u>	<u>Page</u>
Figure 1.1. Location and geological map of study area. ....	2
Figure 1.2. Type and mechanism of scaling observed in TGPP.....	3
Figure 1.3. Structure of CATIN polymer .....	6
Figure 1.4. Structure of -NH <sub>2</sub> terminated PAMAM (a), Carboxymethyl inulin(CMI) (b).....	7
Figure 1.5. Structure of Algea core star shaped polyacrylamide dendrimer. ....	8
Figure 1.6. Structure of polyethylene imine (PEI).....	9
Figure 1.7. Structure of poly(adipic acid/amine-terminated polyether D230/diethylene triamine) (AA/AT/DE) (a), and polyepoxysuccinic acid (PESA) (b).....	9
Figure 2.1. Schematic view of (a) Reflux and (b) Autoclave reactor system. ....	14
Figure 2.2. Polymerization mechanism of PAM (a), PVPA (b) and PVSA (c).....	17
Figure 3.1. Major ions and heavy metals in Tuzla Geothermal Fluid. ....	23
Figure 3.2. Scaling potential of Tuzla Geothermal Field production wells (T9) upon boiling of aquifer fluid a) Silicate, b) Potential deposits. ....	24
Figure 3.3. Scaling potential of Tuzla Geothermal Field production wells (T16) upon boiling of aquifer fluid a) Silicate, b) potential deposits. ....	24
Figure 3.4. SEM images of deposits obtained from a) TGF (vaporizer) ×25k, b) Reflux ×50k, and c) Autoclave ×25k.....	26
Figure 3.5. XRD of deposits obtained from TGF (vaporizer), Reflux, and Autoclave (Magnetite *, NaCl Δ).....	26
Figure 3.6. X-band EPR spectra of TGF and artificial deposits (Trial E and Trial G, latter deposit containing no iron) recorded at room temperature. The spectra of TGF deposit and artificial Trial E sample were normalized to the same iron content (a), X-band EPR spectra of TGF and artificial	

deposits (Trial A, B, C, D, E and F) recorded at room temperature. The spectra were normalized to their maxima (b). ....	28
Figure 3.7. XPS survey spectra of the natural deposit and precipitate obtained from Autoclave system (a) overall, (b) Si 2p and O 1s atoms binding energy.....	30
Figure 3.8. XRD pattern of the deposits obtained from Na Silicate in the presence of various salts given in Table 2.1 (Trial G ( $\text{Na}^+$ , $\text{Ca}^{2+}$ , $\text{Mg}^{2+}$ and $\text{SiO}_2$ ), Trial H ( $\text{Na}^+$ , $\text{Ca}^{2+}$ , $\text{Fe}^{2+}$ and $\text{SiO}_2$ ) and Trial J ( $\text{Na}^+$ , $\text{Mg}^{2+}$ , $\text{Fe}^{2+}$ and $\text{SiO}_2$ )......	32
Figure 3.9. Solubility profiles of (a) $\text{SiO}_2$ , (b) $\text{Mg}^{2+}$ , (c) $\text{Fe}^{2+}$ in the presence of various inhibitors at different dosages. Dashed line refers to the control sample....	34
Figure 3.10. Soluble $\text{SiO}_2$ concentration in the various antiscalants. Only Na-Silicate is used as reactant without having metal salts. For each polymer, most effective dosage in brine trials was used. (PAM: 100 ppm, PVSA: 25 ppm, PVPA: 100 ppm, PAM-co-VSA: 100 ppm, PAM-co-VPA: 25 ppm, PVSA-co-VPA: 50 ppm, PAM-co-VSA-co-VPA: 100 ppm.).....	35
Figure 3.11. FTIR spectrum of pendant group of (a) PAM, (b) PVSA and (c) PVPA with metals (Ca, Mg, Fe), that possibly act as a ligand.....	37
Figure 3.12. Schematic representation of flocculation mechanism in the presence of metal cations and negatively charged polymer. ....	39

## LIST OF TABLES

<u>Table</u>	<u>Page</u>
Table 2.1. Initial concentrations of synthetic brine solutions for Reflux and Autoclave reactors .....	13
Table 3.1. Mass percent composition of deposits obtained from Reflux and Autoclave. TGF results are based on the previous study.....	27
Table 3.2. Binding energies, in eV, for TGF and Autoclave samples, and reference compounds of identified metal salts. ....	31
Table 3.3. Molecular properties and efficiency of silicate solubility of the co/polymers.....	36
Table 3.4. Characteristic absorption bands in the IR spectra of the polymers (PAM, PVSA, and PVPA) and their metal complexes ( $\nu$ , $\text{cm}^{-1}$ ), (resolution: $2 \text{ cm}^{-1}$ ).....	38

# CHAPTER 1

## INTRODUCTION

### 1.1. Geothermal Energy and Scaling Problem

Geothermal energy is a renewable and sustainable energy source. However, the deposition of scale such as silicates and calcite is one of the main handicaps in many geothermal systems, such as the Tuzla Geothermal Power Plant (TGPP), which is located 5 km from the Aegean Sea and 80 km south of the city of Çanakkale, near the ancient city of Aleksandra Troia in northwestern Turkey (Figure 1.1) (Baba et al. 2015, Çelik et al. 2017). The TGPP has an installed power generation capacity of 7.5 MWe and an annual energy production capacity of 51 GWh and is a closed-cycle system. Significant amounts of seawater enter the fault system such that the water is saturated with atmospheric oxygen (Demir et al. 2014). Moreover, the power plant experiences stoppages five times per year, and the system is opened for cleaning and maintenance during this process. Therefore, the system is not free from oxygen.

Scaling problems substantially reduce the efficiency of geothermal power plants and cause financial losses (Baba et al. 2015, Demir et al. 2014). The deposition of scale and related phenomena are considered as major constraints on the improvement of geothermal energy. At the core of the earth, the high temperature and pressure cause some rock to melt, creating magma convection upward since heats water and rock in the crust. While, geothermal fluids are pumped from down to top the conditions of the brine are changing (Dogan et al. 2014). Decreasing temperature and pressure causes increase in the pH. Silicate, carbonate and sulfonate scaling occurs with increasing level of pH. In addition to this, silica gives reactions with metal-oxides to more stable complexes (Gallup 1997). Calcite scaling is well known and can be solved with commercial inhibitors. Unfortunately, silicate scale can't be solved with an inhibitor yet and causes to clogging in geothermal power plant's components. The yield of electricity decreases and during the cleaning process the system is shut-down.

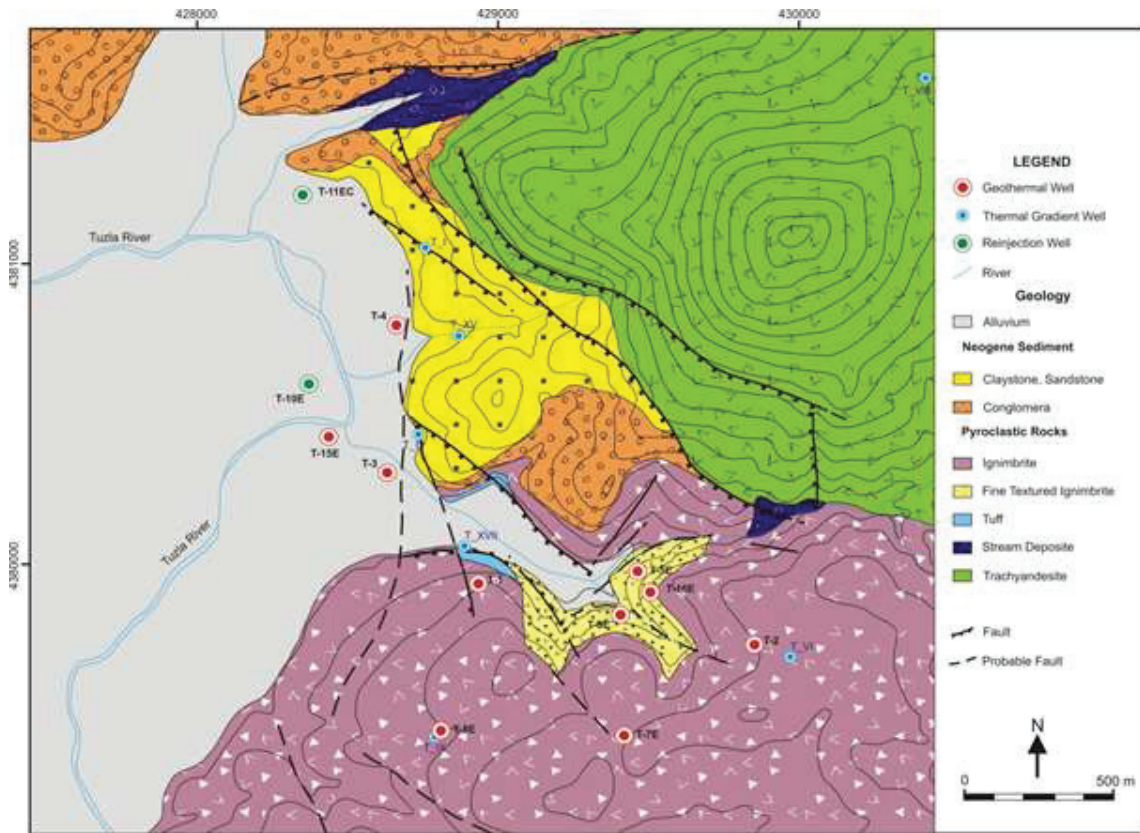


Figure 1.1. Location and geological map of study area.  
(Source: Baba et al. 2015, WES JEC 2006)

## 1.2. Types of Scaling

Among the different minerals liable to be deposited, silica is a common component and is difficult to remove. Silica precipitates in many different forms in nature (e.g., quartz, tridymite, cristobalite, amorphous silica, etc.) (Ehrlich et al. 2010, Ghoul et al. 2015). Although quartz is mainly observed in nature, extensive deposits of amorphous silica are found to have formed in the Tuzla Geothermal Field (TGF) (Baba et al. 2015, Çelik et al. 2017, Demir et al. 2014, Dogan et al. 2014). Soluble form of monosilicic acids combine and form tetramers. After the tetramerization of linear silicic acids have become cyclic structure till they reach to a critical mass. While tetramerization process, oxide forms of metal cations are also formed with increasing pH and soluble silica become no more soluble (Demadis and Neofotistou 2004). Finally, amorphous silica precipitates in the form of metal silicate deposits that contain mainly iron and magnesium ions, which are very hard and dense and are difficult to remove from geothermal systems. The type of scaling in TGPP and mechanism is explained in Figure 1.2 (Çelik et al. 2017).

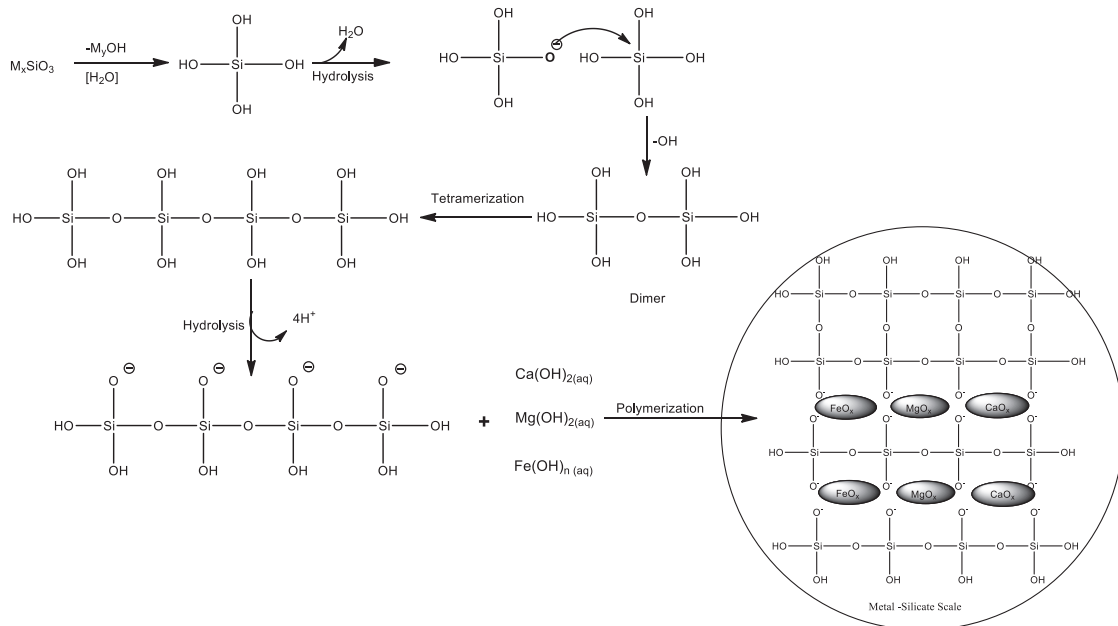


Figure 1.2. Type and mechanism of scaling observed in TGPP.

### 1.3. Literature Review

#### 1.3.1. Mechanism of Scaling

The association of silicate solutions with metal salts has been documented in the literature. Saishu, Okamoto, and Tsuchiya (2013), for instance, examined the effect of a mixture of  $Na^+$  and  $Al^{3+}$  on the morphology and precipitation rates of silica deposits. The experiments were performed with a constant Na/Al ratio of 1.48 and increasing  $Al^{3+}$  concentrations from 0 to 6.7 ppm. According to the results, the precipitation rate and the amount of silica precipitated increased with increases in the concentration of  $Al^{3+}$  and  $Na^+$ . These ions might promote the formation of Na-Al-Si complexes in solution. Moreover, with increases in the amount of these ions the morphology of the precipitates was found to be modified. Although at low  $Al^{3+}$  concentrations amorphous silica was formed, at higher concentrations of  $Al^{3+}$  the amorphous structure was transformed into quartz. This result was attributed to a reduction in the energy barrier required for the nucleation of quartz to occur. In another study, Icopini, Brantley, and Heaney (2005) investigated the effects of various parameters, such as ionic strength, pH, and different initial concentrations of silica, on the rate of oligomerization of silica. The ionic strengths

of all solutions were obtained using a mixture of  $\text{Na}^+$ ,  $\text{K}^+$ ,  $\text{Ca}^{2+}$ ,  $\text{Cl}^-$ , and  $\text{HCO}_3^-$  solutions. Test experiments were carried out at ionic strengths of 0.01 and 0.24 molal (m), pH values ranging from 3 to 11, and initial concentrations of silica of 250, 750, and 1250 ppm. The results showed that silica nanocolloids were stabilized at low pH and low ionic strengths but became unstable when the solution pH was near neutral and at higher ionic strengths and higher initial silica concentrations. The rate of oligomerization of silica was higher by six orders of magnitude in solutions with high ionic strengths than in those with low ionic strengths. Moreover, the rate increased with an increase in the initial concentration of silica. Chen and Marshall (1982) stated that  $\text{Na}_2\text{SO}_4$ ,  $\text{NaCl}$ ,  $\text{MgSO}_4$ , and  $\text{MgCl}_2$  affected the concentration of dissolved silica. Increases in the salt concentration increased the amount of silica precipitated. In addition, the effect of temperature on scaling by silicates was examined, where the experiments were conducted at constant salt concentrations. The results showed that the solubility of silica increased with an increase in temperature. In addition, the effects of added salts and temperature were found to change the structure of the precipitate, which underwent a transformation from amorphous silica to cristobalite or quartz. Gallup et al. (2003) studied the desilication of geothermal water systems to obtain more commercially valuable minerals. The experiments were performed at 90 and 130 °C. Except for  $\text{Mg}^{2+}$ , other cations reacted with silica to give poorly crystalline metal-rich silicates and co-precipitated as metal carbonates at 90 °C. Raising the temperature to 130 °C resulted in an increase in the crystalline content of the precipitates, which suggested the formation of more commercially valuable minerals. The results of desilication tests showed that the most effective desilicating agents were  $\text{Mn}^{2+}$  and  $\text{Fe}^{2+}$ . Silica precipitated rapidly with the use of these cations, and a combination of  $\text{Mg}^{2+}$  and  $\text{Fe}^{2+}$  in solution reacted with silica to give saponite-type precipitates. Brown (2011) examined the thermodynamics and kinetics of scaling by silica. His group performed test experiments on scaling by silica using  $\text{NaCl}$  solutions. As the supersaturation index increased, the rate of precipitation of silica also increased. This result was explained by a reduction in the electrostatic attraction between  $\text{Na}^+$  and monosilicic acid. Silica colloids in dilute solutions were very stable and had negative surface charges that prevented the agglomeration of silica particles. If the concentration of the solution reached supersaturation, cations surrounded the negatively charged silica particles, with the results that cations in saturated solutions and silica particles came together to form metal silicate precipitates, negatively charged silica particles approached closer to each other, and larger silica colloids formed.

### **1.3.2. Inhibitor Chemistry**

Silicate scaling in TGPP has detrimental effects on the production performance and components of the system (Dogan et al. 2014). To get rid of such stubborn scale that formed in perforation holes, vaporizer, separator, etc. the power plant is shut down and cleaning with HF (Baba et al. 2015). HF is a strong acid so damage the power plant's components and harmful for the human health. Metal-silicate scaling have been occurring with increasing pH because of the releasing the soluble CO<sub>2</sub> from the brine. Soluble carbon dioxide has been passing to the vapor phase with decreasing pressure and temperature. To recover the acidity of the brine, formic acid has been adding. This solution is the best short-term remedy, but inhibition or dispersion of metal-silicate scaling is required (Baba et al. 2015, Demadis 2012, Demadis et al. 2007, Demadis and Neofotistou 2004, Gallup 1997, 1998, 2002).

Metal-silicate deposits can be formed in many different forms that depends on the content of the brine (Ståhl et al. 2000, Gunnlaugsson and Einarsson 1989, Kristmannsdóttir 1989, Ghoul et al. 2015). (Fe,Mg) silicate can't be removed easily and has a rigid and dense structure. Although the mechanism and kinetic's of condensation reaction of silicic acid is not well known, amorphous silica has been forming by the nucleophilic addition of soluble silicic acid molecules and precipitates after reaching to the critical mass (Demadis and Neofotistou 2004, Matijević and Goia 2007). Monosilicic acid condensed and formed dimers, trimers and tetramers. After tetramerization they form tiny cyclic structures and agglomerates. Agglomeration is continuing till they reach to a critical mass. During this process, oxide forms of metals are forming because of increasing pH and penetrates in to the cyclic silica network (Çelik et al. 2017). Finally, layered (Fe, Mg) silicate is forming and continue to plug till the cleaning time. Metal-silicate scaling remediation is required not only dispersion/inhibition of negatively charged silica particles, but also metal cations in brine should be mitigated. The interaction between anionic silica particles and macromolecules and their dosages have been employed by many scientists to test silica inhibition performances. End group of macromolecule and the concentration has critical role. (Chauhan et al. 2014, Zhang, Chen, and Li 2011, Brinker and Scherer 2013, Sjöberg 1996, Amjad and Demadis 2015) Antiscalants have been employed recently for the brine treatment. They are commonly (Gallup 2002, Gallup and Barcelon 2005) macromolecules such as polymers and dendrimers (Chauhan et al. 2014) containing cationic part constitute important class of

silica scale inhibitors such as cationic inulin and polyaminoamide (PAMAM). Ketsetzi, Stathoulopoulou, and Demadis (2008) worked on CATIN (cationic inulin) polymer has quaternary ammonium cationic charge with its different degree of substitution (DS, average number of cationic groups per monomer) values and tested for silica inhibition efficiency. DS values of CATIN 1, 2 and 3 polymers were 0.22, 0.86 and 1.28, respectively. Different dosages of CATIN (Figure 1.3) were tested at 40, 80 and 100 ppm. In the light of test experiment results, the inhibition performance associated with dosage and DS values. Although 100 ppm dosage level showed detrimental effect on silica inhibition performance by forming flocculants because of interaction between poly anion and poly cations, at 40-ppm dosage level gave the best result with CATIN 2 and 3 (DS= 0.86 and 1.28) polymers. Main topic in this article is CATIN polymers show inhibition activity but their performances mainly dependent with the number of cationic charges on monomer unit and applied dosage level (Ketsetzi, Stathoulopoulou, and Demadis 2008).

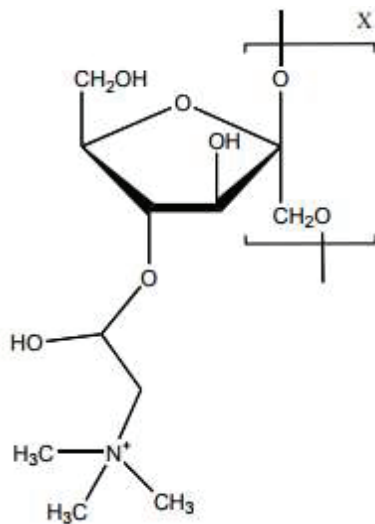


Figure 1.3. Structure of CATIN polymer.  
(Source: Ketsetzi, Stathoulopoulou, and Demadis 2008)

Dendrimers were tested in many studies because of their structural advantages. PAMAM dendrimer's main structural property explained as branches with different growth generations and chemical group modifications around a central core. In this study Demadis et al. (2005) were tested the inhibition efficacy of PAMAM dendrimers (Figure 1.4a) which had different groups and generations were tested. PAMAM 1 and 2 has -NH<sub>2</sub> termini and, PAMAM 0.5, 1.5 and 2.5 had -COOH terminated groups. The test experiments were performed with 500 ppm SiO<sub>2</sub> solution and 40 ppm dosage of each

PAMAM dendrimers at pH 7. The results were monitored per 24 h for 72 h. Control, PAMAM 0.5, 1.5 and 2.5 and, PAMAM 1 and 2 test experiments showed 171 ppm, ~200 ppm and ~380 ppm, respectively for 24 h. COOH terminated PAMAM dendrimers were showed no significant inhibition activity in contrast to NH<sub>2</sub> termini (PAMAM 1 and 2) dendrimers showed a remarkable soluble silicate level increase comparing to control experiment. The test experiments of PAMAM 1 and 2 resulted in ~310 ppm soluble silicate levels after 72 h, but white flocculants were also observed. All in all, the effect of COOH groups is insignificant because of repulsive forces between anionic silica particles and deprotonated COO<sup>-</sup> groups.

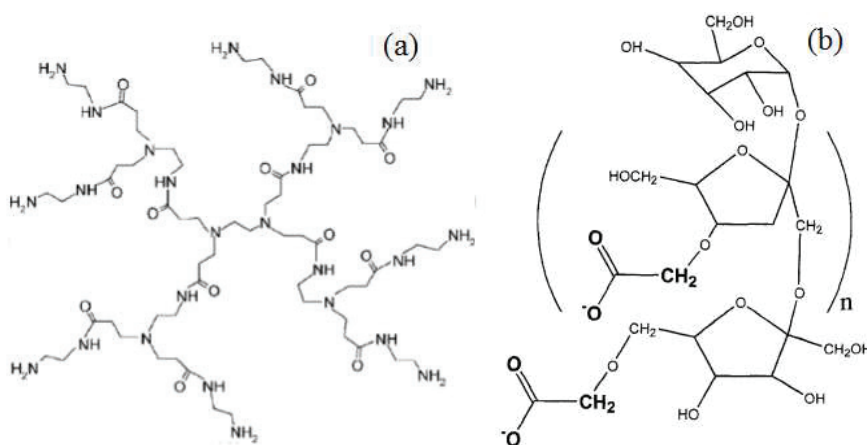


Figure 1.4. Structure of -NH<sub>2</sub> terminated PAMAM (a), Carboxymethyl inulin(CMI) (b).  
(Source: Demadis et al. 2005)

Although PAMAM 1 and 2 dendrimers' performances were promising, the formation of white flocculants is the evidence to the loss of their inhibition performances in time. Because cationic protonated -NH<sub>3</sub><sup>+</sup> groups attract and entrap with anionic silicate groups. The comparison of -NH<sub>2</sub> terminated between PAMAM 1 and 2 showed a better result with PAMAM 1 dendrimer. All in all, PAMAM dendrimers' inhibition or retardation performances are structural and end group dependent. In the previous study the inhibitory performance of -NH<sub>2</sub> terminated dendrimer was studied. The flocculation effect of PAMAM-SiO<sub>2</sub> complex was the main problem. To prevent this detrimental complex formation, a anionic polymer was added (Demadis and Neofotistou 2004). Demadis and his co-workers performed a study to improve inhibition efficacy of PAMAM dendrimer by adding Carboxymethylinulin (CMI) polymer (Figure 1.4b). Anionic groups of deprotonated -COO<sup>-</sup> on CMI were neutralized -NH<sub>3</sub><sup>+</sup> groups on PAMAM and was prevented the cooperation of -NH<sub>2</sub> groups and SiO<sub>2</sub> matrix which was

resulted as deactivation. Above the 40 ppm dosage level of CMI, improvement of inhibition performance of PAMAM was detrimental.

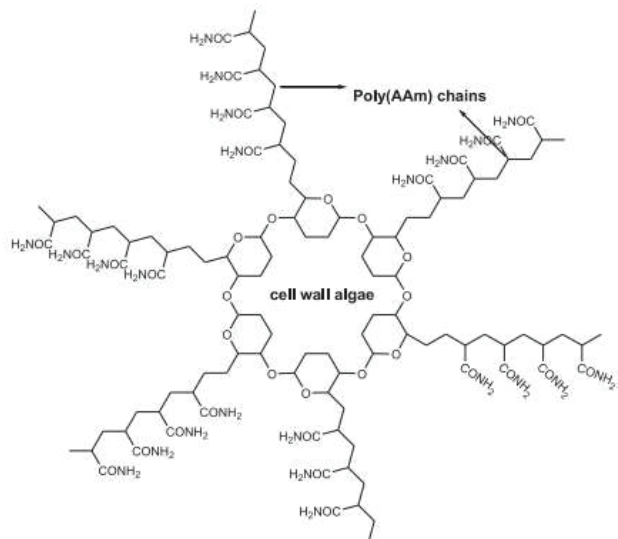


Figure 1.5. Structure of Algea core star shaped polyacrylamide dendrimer.  
(Source: Chauhan et al. 2014)

According to the literature, potential silica inhibitors have amine structural units. In the light of this information Chauhan et al. (2014) tested silica scale inhibition activity of a bio-inspired algae core which was modified with polyacrylamide and polyacrylicacid star shaped polymers (Figure 1.5) with different dosages and temperatures. The test experiments were done at 35 °C and 55 °C for 20, 60 and 80 ppm dosage levels. Higher temperature value test experiments were showed lower soluble silica levels. Moreover, algae core polyacrylamide stars shaped polymer had better inhibition efficiency (~95%) with any flocculants formation for the first 12 h and inhibition performance was increased with increasing polymer dosage (Chauhan et al. 2014).

PAMAM dendrimers' inhibition performances were compared in many studies. One of the interesting studies was the inhibitory efficacy of polyethyleneimine (PEI) with respect to PAMAM dendrimer. Demadis and Stathoulopoulou (2006) were continued to explore structural and amine group effect on silica scale inhibition. PEI's branched structure (Figure 1.6) possesses 50% secondary, 25% primary and tertiary amines and these groups were protonated at pH 7 where test experiments were done.

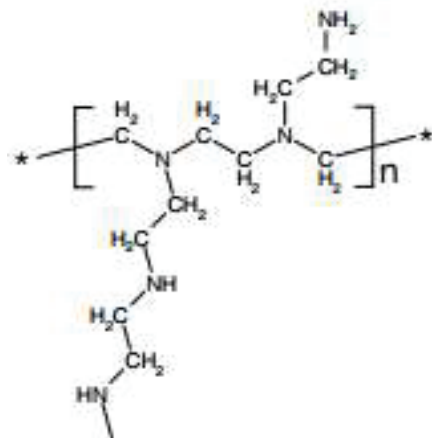


Figure 1.6. Structure of polyethylene imine (PEI).  
(Source: Demadis and Stathoulopoulou 2006)

The cationic charge density on polymer is directly effects the inhibition performance. According to the results, 10 ppm PEI dosage level was showed the best inhibition activity and comparing to PAMAM dendrimer its inhibition performance was insignificant (~250 ppm). The higher the cationic charge densities were resulted as poly cation- anionic silica entrapment and precipitation (Demadis et al. 2007, Demadis and Stathoulopoulou 2006).

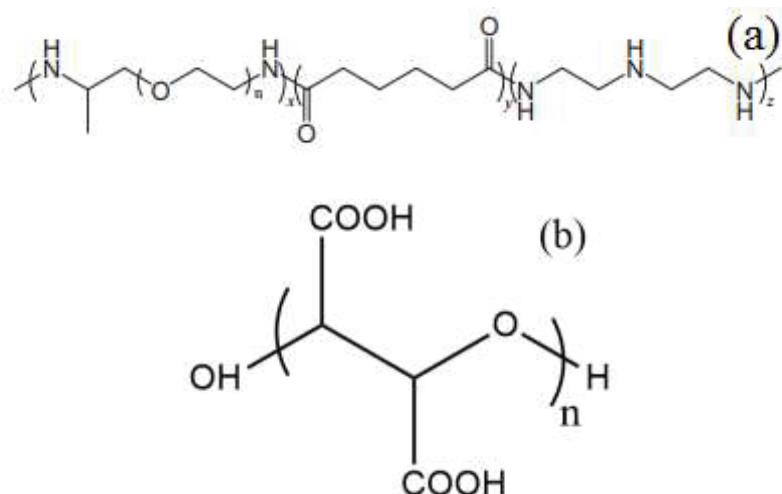


Figure 1.7. Structure of poly (adipic acid/amine-terminated polyether D230/diethylenetriamine) (AA/AT/DE) (a), and polyepoxy succinic acid (PESA) (b). (Source: Zhang et al. 2013)

Zhang et al. was performed to test the inhibition activity of adipic acid/ amine terminated polyethers D230/ diethylenetriamine copolymer (AA/AT/DE) (Figure 1.7) on anionic silica. AA/AT/DE has mainly positively charged -NH- groups that is made it a

potential silica inhibitor. The test experiments were done and concluded that excess positive charge density resulted as formation of white flocculants. To get rid of this floc formation, an anionic poly epoxy succinic acid (PESA) molecule was added. PESA neutralized the positive charges on AA/AT/DE molecule and the best inhibition efficiency reached with a blend of PESA (20 ppm) and AA/AT/DE (40 ppm). Above 20 ppm PESA the effect on silica inhibition was unchanged for 40 ppm and detrimental for 60 ppm (Zhang, Chen, and Li 2011).

#### **1.4. Aim of the Study**

A methodology for testing the performance of potential inhibitors in laboratory conditions is needed. In this study, synthetic precipitates were produced that had similar compositions and morphologies to those of the deposits collected in the vaporizer of the TGPP. Synthetic brine consisting of Cl-rich salts of the common metal ions  $\text{Fe}^{2+}$ ,  $\text{Mg}^{2+}$ , and  $\text{Ca}^{2+}$  in the presence of Na silicate and Na carbonate was prepared and reacted at high temperatures. Two types of apparatus (reflux and autoclave) were employed for the fabrication of metal deposits. Refluxing is a technique commonly used in chemistry laboratories and can be used as a screening technique for potential inhibitors. On the other hand, an autoclave is a more specialized apparatus in which it is possible to increase and control pressure, pH, and temperature during the synthesis of artificial deposits. The formation of deposits in the autoclave reactor was found to be close to the field conditions, which was a prerequisite for screening potential inhibitors of scaling by metal silicates. The resulting deposits were characterized in terms of elemental composition, morphology, crystal structure, and structural formation. The experimental conditions were adjusted to enable the fabrication of deposits of which the features closely resembled those of naturally observed deposits, to confirm the efficacy of the inhibition performance of potential organic compound inhibitors. Although the silica scaling inhibitors exhibit promising effect, they are less effective for metal-silicate scaling (Gallup et al. 2003, Icopini, Brantley, and Heaney 2005). The presence of metal cations, i.e. water hardness triggers the rate of metal silicate precipitation compared to normal (soft) waters. The soluble silica concentrations were tested with different Ca:Mg ratio solutions (Demadis et al. 2005). For this reason, the effect of metal contribution will be the main focus to inhibition of metal-silicate scaling. Water-soluble polymers that contain ligands on main or side chain such as sulfonic acid, phosphonic acid, and acrylamide were synthesized for

the removal of metal ions (Girma et al. 2005, 2006, Palencia, Rivas, and Pereira 2009, Rivas et al. 2004). These polymers can form either, monodentate and bidentate metal-ligands or directly bonded. The important requirements of these polymers can be sort as solubility in water, route of synthesis, chemical stability and affinity to metal ions. In this study, we synthesized homo and copolymers of functional comonomers of vinyl sulfonic acid sodium (VSA), vinyl phosphonic acid (VPA), and acrylamide (AM). The antiscaling performance of three homopolymer, three copolymers, and one tercopolymer was examined at various dosages taking into account of solubility of silica and metal cations.

## CHAPTER 2

## EXPERIMENTAL

### 2.1. Materials and Methods

For the synthesis of artificial metal silicate deposits, two different types of apparatus were used, namely, reflux and autoclave systems. The former included a round-bottom flask heated to 90 °C under atmospheric conditions. A Radleys Carousel 6 Plus Reaction Station (Saffron Walden, UK) was used as the reflux system (Figure 2.1a). A 075 miniclave (Buchiglasuster, Uster, Switzerland) was used as the autoclave reactor (Çelik et al. 2017). This reactor had three main components: a main skeleton, a circulator device, and a monitor. The main skeleton comprised a closed container, liquid and gas inlets, a magnetic mixing motor, and temperature and pH probes (Figure 2.1b). The closed container was made of glass and consisted of two layers. Hot silicone oil was introduced between these layers and removed by the circulator device at temperatures of up to 250 °C. The magnetic mixing motor stirred the reaction solution uniformly at speeds of up to 3000 rpm. Three of the inlets/outlets on the closed container were used for the circulation of silicone oil and one of them was used to remove the heated solution. Values of temperature and pH (up to 100 °C) were measured with the probes and displayed on the monitor screen. To mimic natural scale formed in TGPP,  $\text{FeCl}_2 \cdot 4\text{H}_2\text{O}$  and  $\text{MgCl}_2 \cdot 6\text{H}_2\text{O}$ , which were purchased from Merck (New York, USA),  $\text{CaCl}_2$  and  $\text{Na}_2\text{CO}_3$ , which were obtained from Sigma-Aldrich (St. Louis, MO, USA), and  $\text{Na}_2\text{SiO}_3$  (35.5 wt.% in  $\text{H}_2\text{O}$ ), which was purchased from Carl Roth (Karlsruhe, Germany) chemicals were used.

Acrylamide, vinyl sulfonic acid sodium (VSA) solution (wt.25%) and vinyl phosphonic acid (VPA) were used as comonomers for polymer synthesis. Ammonium persulfate and 4,4'-Azobis (4-cyanovaleic acid) (ACVA) were used as an initiator. Polymer chains were precipitated in the presence of equivolume mixture of methanol and acetone. All these chemicals and solvents were purchased from Sigma Aldrich and were used as received without any further purification. The deionized water ( $18.2 \text{ M}\Omega \cdot \text{cm}^{-1}$  at 25 °C) used in all experiments was produced by Milli-Q Advantage.

## 2.2. Synthesis of Artificial Metal Silicate Deposits

The precipitates were synthesized from synthetic brine, which was prepared by mixing equal volumes of solutions of chlorine salts of iron, magnesium and calcium, and sodium silicate and sodium carbonate. Reagent-grade Na silicate solution was diluted with distilled water (13.2 mS/cm at 25 °C) to yield a concentration of approximately 2 g/L SiO<sub>2</sub>. The initial concentrations and conditions of the artificial brine solutions are given in Table 2.1, nine trials are reported. Last three trials were done to test the catalytic effect of divalent cations on the silicate precipitation. The pH of the reaction mixture was about 8.0 and no adjustments were made.

Table 2.1. Initial concentrations of synthetic brine solutions for Reflux and Autoclave reactors.

Ions	Trial	Initial Concentrations (ppm)					Conditions
		[Fe <sup>2+</sup> ]	[Mg <sup>2+</sup> ]	[Ca <sup>2+</sup> ]	[Na <sup>+</sup> ]	[SiO <sub>2</sub> ]	
Reflux	A	927	404	665	600	285	90 °C,
	B	927	404	1330	1147	1000	1 bar
	3C	927	404	1330	1912	2000	
Autoclave	D	927	404	665	600	285	
	E	927	404	1330	1147	1000	137.6 °C,
	F	927	404	1330	1912	2000	3.2 bar
	G	-	404	1330	1912	2000	
	H	927	-	1330	1912	2000	
	J	927	404	-	1912	2000	

An aliquot of 100 mL synthetic brine solutions (first part of Table 2.1.) were placed in the reflux system at 90 °C and was mixed at 200 rpm. After 6 h, the reaction mixture was left to cool slowly to room temperature. The reaction mixture consisted of solid particles in an aqueous solution, which were isolated via centrifugation, and the leftover solution was collected.

The synthetic brine solutions were placed in the closed container of the autoclave reactor system (second part of Table 2.1.). Prior to the reaction, air at a pressure of 1 bar was loaded into the system. The reaction was completed after about 45 min. The final pressure and temperature values were 3.2 bar and 137.6 °C, respectively. The reaction solution was removed with a Teflon pipe and collected in a plastic bottle which was placed in an ice-water bath to shock the reaction solution. After 2 h, the solution containing the precipitate was taken and centrifuged to separate the precipitate (deposit) from the decantate. The deposit was dried in an oven at 140 °C for 4 h. Both solid and liquid samples were subjected to characterization separately.

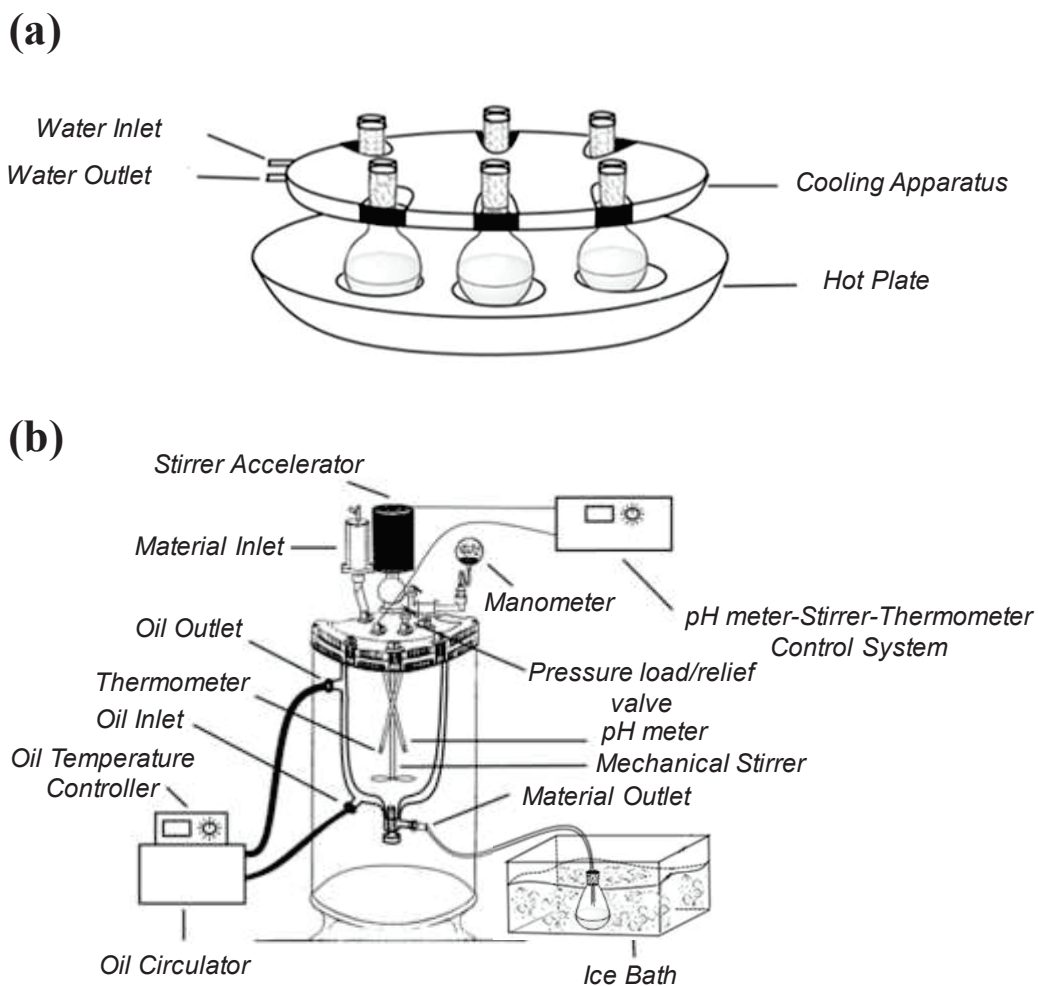


Figure 2.1. Schematic view of (a) Reflux and (b) Autoclave reactor system.

### **2.2.1 Effect of Metal Cations**

The effect of metal cations was tested in last three trials in Table 2.1. Each trial consists of the absence of one of the divalent metal cation. The catalytic effect of metal ions was known from the literature (Brown 2011, Chen and Marshall 1982, Kristmannsdóttir, Ólafsson, and Thórhallsson 1989, Saishu, Okamoto, and Tsuchiya 2013), to understand this effect the morphology and texture of the precipitates and concentrations of soluble silicic acid in decantate were monitored.

Equal 40 mL volumes of solutions were mixed and completed to 200 mL with distilled water, and then reacted under the same conditions of 3.2 bar and 137.6 °C. The results for both decantates and deposits were compared with those of Trial F, which gave the closest features to those of deposits.

## **2.3. Characterization of Brine and Decantate**

Geothermal fluids were taken from wells (T8, T9, and T16) and springs (S-2, S-11, TS-1, TS-3, ES-1, ES-4, and ES-6) during the wet and dry seasons in the TGF. For the analyses of major ions and trace metals, 1 L plastic bottles were used. To prevent the formation of complexes of trace elements with oxygen, samples were filtered using 0.45 µm filter paper and acidified to a pH of  $\leq 2$  by adding 0.5 N HNO<sub>3</sub> in the field. Chemical analyses of major cations and heavy metals were carried out using inductively coupled plasma atomic emission spectrometry for B<sup>3+</sup>, Ba<sup>2+</sup>, Cr<sup>2+</sup>, Fe<sup>2+</sup>, Li<sup>+</sup>, Pb<sup>2+</sup>, and Zn<sup>2+</sup>, etc., whereas SO<sub>4</sub><sup>2-</sup>, Cl<sup>-</sup>, Ca<sup>2+</sup>, Mg<sup>2+</sup>, Na<sup>+</sup>, and K<sup>+</sup> were determined by ion chromatography, and HCO<sub>3</sub><sup>-</sup> concentrations were determined by titration.

For the decantates, spectroscopic techniques were used to determine the ion concentration. Soluble SiO<sub>2</sub> was assayed via the silicomolybdate UV colorimetric method with a Hach DR 5000 spectrophotometer (Colorado, USA) using the 656 Silica HR program. Cations in the decantate (Fe<sup>2+</sup>) were measured via inductively coupled plasma–mass spectrometry (ICP-MS) with an Agilent 7500 ce Octopole (Santa Clara, USA) and (Na<sup>+</sup>, Ca<sup>2+</sup>, Mg<sup>2+</sup>) via ion chromatography (IC) Thermo Scientific Dionex ICS 5000 (Massachusetts, USA) instrument.

## **2.4. Characterizations of Natural Scale and Artificial Deposits**

Both of natural and artificial synthesized samples were powdered with a mortar and subjected to characterization using X-ray diffraction (XRD), X-ray fluorescence, scanning electron microscopy (SEM), X-ray photoelectron spectroscopy (XPS), and electron paramagnetic resonance (EPR). The crystal structure, morphology, elemental composition, binding energies, and paramagnetism of the deposits were determined and compared using XRD (Philips X’Pert Pro, Eindhoven, The Netherlands) ( $2\theta = 5\text{--}80^\circ$ , std.), SEM (FEI Quanta 250 FEG, Oregon, USA) (the sample was covered with gold under vacuum), XRF (Spectro iQ II, Kleve, Germany) (mass loss on fusion), XPS surface analysis (K-Alpha, Massachusetts, USA), and EPR (Adani CMS 8400, Minsk, Belarus) (20 dB), respectively.

## **2.5. Synthesis of Polymers**

Polyacrylamide, poly (vinyl sulfonic acid) and poly (vinyl phosphonic acid) were synthesized according to the chain growth polymerization mechanism. Polymerization reaction mechanism was represented in Figure 2.2.

Acrylamide was dissolved in distilled water and reacted with APS. After a while, viscous solution was precipitated with methanol and dried. VSA-Na salt was polymerized with APS by radicalic addition polymerization mechanism (Okayasu et al. 2009). The liquid precipitated with a proper solvent and dried. VPA was diluted and reacted with ACVA (Macarie and Ilia 2010, Bingöl et al. 2006). To get rid of left over unreacted monomer, the solution dialyzed.

To synthesize copolymer and tercopolymer of PVSA, PAM and PVPA, proper monomers were mixed and reacted with a suitable initiator. APS was used as initiator for the synthesis of Polyacrylamide-co-(vinyl phosphonic acid) (PAM-co-VPA), Polyacrylamide-co-(vinyl sulfonic acid) (PAM-co-VSA), Poly(vinyl sulfonic acid)-co-(vinyl phosphonic acid) (PVSA-co-VPA) and Polyacrylamide-co-(vinyl sulfonic acid-co-vinyl phosphonic acid) (PAM-co-VSA-co-VPA). The temperature was kept optimum where the decomposition of initiator is maximum.

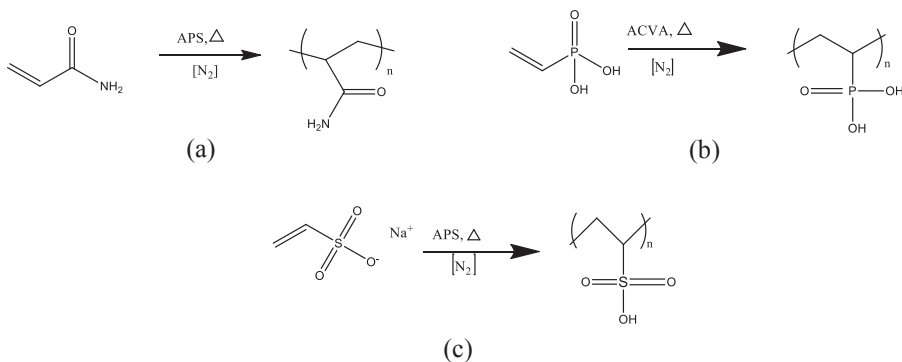


Figure 2.2. Polymerization mechanism of PAM (a), PVPA (b) and PVSA (c).

## 2.6. Characterization of Polymers

Chemical structures of polymer chains were supported by <sup>13</sup>C and <sup>1</sup>H NMR analysis which were performed by Variant V NMR 400. Effect of polymers was investigated both in decantate and precipitate.

Molecular weight of polymers was measured by Static Light Scattering (SLS) method. This method is described as measuring the sample at various concentrations and applying the Rayleigh equation. For a calculation, the differential refractive index increment ( $dn/dC$ ) of each polymer was measured by Abbe type refractometer.

## 2.7. Inhibitor Tests

Inhibitory effect of polymers was examined on artificial brine recipe given in Table 2.1. The scales were synthesized from synthetic brine solution that contains equal volume (40 mL) of each of FeCl<sub>2</sub>·4H<sub>2</sub>O, MgCl<sub>2</sub>·6H<sub>2</sub>O, CaCl<sub>2</sub>, Na<sub>2</sub>CO<sub>3</sub>, and Na<sub>2</sub>SiO<sub>3</sub> solutions. Initially, artificial brine solution was injected into the autoclave, and reaction was maintained at 137.6 °C and 3.2 bar for 45 min. Polymer solutions (50 mL) were added to mixture in various concentrations (25, 50, and 100 ppm) during evacuation from autoclave system. The mixture was cooled in ice bath for 2 hours after polymers were added. The precipitate was isolated by centrifugation (6000 rpm, 30 min). The leftover solution is analyzed by spectrophotometer, ICP-MS and IC.

The criteria for success of polymeric metal-silicate inhibitor is solubility of silica that is provided by mitigation the reaction between cations and silicic acid. To indicate this success in mathematical definition, we used the formula, which is given below:

$$n = \frac{C_1 - C_2}{C_{max} - C_2} \times 100 \quad (2.1)$$

where  $C_1$  and  $C_2$  refer to  $\text{SiO}_2$  concentration in the presence and absence of polymeric metal-silicate inhibitor respectively.  $\text{SiO}_2$  concentration in the absence of metal cations is expressed as  $C_{max}$  and is experimentally measured as 408 ppm. In the decantate, soluble  $\text{SiO}_2$  were measured by UV-silica molybdate colorimetric method with Hach DR 5000 instrument using 656 Silica HR mode. Concentration of the cations in decantate ( $\text{Fe}^{2+}$ ) were measured by ICP-MS technique and ( $\text{Na}^+$ ,  $\text{Ca}^{2+}$ ,  $\text{Mg}^{2+}$ ) via IC instrument.

## 2.8. Characterization Tools

### 2.8.1. Inductively Coupled Plasma-Mass Spectrometry (ICP-MS)

Inductively coupled plasma mass spectrometer is used for the analytical determinations. This instrument provides good solution for the determination of rare-earth elements with ppb level of limit of detection values. Maximum detection limit value is about 1 ppm. Determination of cations and their isotopes is available with this technique, unfortunately anions measurements are not reliable. Plasma source of the instrument (Argon) converts the elements to ions that are separated with respect to their mass-to-charge ratios by the radio frequency generator. Finally, they can be detected in mass spectrometer part by quadrupole mass filter (Wolf 2005).

### 2.8.2. Ion Chromatography (IC)

Ion chromatography is a separation technique, which can determine anionic and cationic inorganic species, low molecular weight water soluble organic molecules and organic bases. Measurement of molecules is based on ion mobility of their conductivity properties. Retention time of molecule is detected and area under the peak determines the concentration of the solute. It is good separation method inorganic ions with the help of reversed phase columns. The technique requires a good selection of stationary and eluent phases which can provide reliable and accurate measurements (Haddad and Jackson 1990).

### **2.8.3. UV-Silicomolybdate Spectrophotometry**

Ultra-violet spectroscopy technique is based on the determination of absorbance values of the sample. Light pass through to the sample and some of them are reached to the detector. If the light is absorbed by the sample, the intensity of the detected light is less than incident light. According to the Beer's Law, there is a direct relation between absorbed light and detected species concentration. To apply this law, a spectrophotometer (or colorimeter) is required (Clark, Frost, and Russell 1993).

Ammoniummolybdate molecule is chelated with soluble SiO<sub>2</sub> molecule and yellow color is observed in the presence of this complex formation. A spectrophotometer can measure the concentration of SiO<sub>2</sub>-molybdate complex up to 100 ppm detection limit value at a specific wavelength (452 nm).

### **2.8.4. X-Ray Diffractometer (XRD)**

It is a non-destructive analytical technique and based on the diffraction of bombarded x-ray beam. Scattered x-ray beam reaches to the detector with regular patterns if the material has crystalline structure. Since, crystalline structure has uniform and parallel rows between atoms with a unique distance. The direction of scattered x-ray beam depends on the lattice structure of material. Diffraction occurs if the structure is crystalline and x-ray beam scatters. This phenomenon provides a qualitative information about the substances. In contrast to crystalline ordered structure, radiation beam pass through the material if has amorphous structure and give unmatched signals (Whittig and Allardice 1986).

### **2.8.5. X-Ray Fluorescence (XRF)**

X-ray fluorescence technique is an analytical method and is based on the interaction between atoms and radiation. Highly energetic (short wavelength) radiation excites the electrons of atoms. If its energy sufficiently high enough to dislodge an electron from the inner shell of the atom, the electron of the outer shell replaces to the missing one. Binding energy of outer shell electron is lower than the inner one, so excess energy is released and emitted as fluorescent radiation. Analysis of both solid and liquid

samples is possible and two different methods can be used. First one is powder analysis which is non-destructive method. Secondly, measurements can be made with loss of fusion, that based on the conversion of material to glass with lithium borate and it is a destructive method. Instrument has limitations that can't analyze  $Z < 11$  (Bernal and Lozano-Santacruz 2005).

### **2.8.6. Scanning Electron Microscope (SEM)**

Scanning electron microscopy technique can provide qualitative information of the sample's surface. The imaging process performed with a focused beam of high energetic electrons to a selected area of the specimen. The interaction between sample and bombarded electrons is detected and revealed the morphology, orientation of materials and semi-quantitative information about the chemical composition of the surface (Swapp 2012).

### **2.8.7. X-Ray Photoelectron Spectrometer (XPS)**

X-ray photoelectron spectroscopy is an analytical technique and provide information of the sample's surface chemical composition. The principle of the measurement based on the analysis of emitted electron. Electron beam bombardment interact with inner shell electron of the specie, emitted electron collides to the detector with a specific kinetic energy. The binding energy of electron is calculated by subtracting kinetic energy of electron from the total x-ray energy. Each atom and their states have different binding energy value, so the chemical and structural composition of the material can be identified with high accuracy (Chastain, King, and Moulder 1995).

### **2.8.8. Electron Paramagnetic Resonance Spectrometer (EPR)**

EPR spectroscopy is one of the powerful method of indicating the presence of paramagnetic transition metal ions (Akdogan et al., 2008). The measurement is based on the absorption of electromagnetic radiation that explained as the interaction of unpaired electron of an atom with magnetic field. EPR spectrometer measure the energy difference generated in the presence of magnetic field.

### **2.8.9. Nuclear Magnetic Resonance (NMR) Spectroscopy**

Nuclear magnetic resonance spectroscopy is an analytical and non-destructive technique. The structure and conformation of organic compounds can be identified with this method and based on presence of magnetic field energy is transferred to the electrons to higher energy levels. When it returns its ground state the absorbed energy emitted and the signals are observed (Harris 1986).

### **2.8.10. Dynamic Light Scattering (DLS)**

Dynamic light scattering instrument measures the particle size of a molecule in a solution or suspension. It is an analytical and spectroscopic technique that based on the measurement of intensity of scattered light from the specie as a function of time. This technique is useful for the characterization of hydrodynamic radius of polymers/or proteins and determination of the size distributions of nano particles (Tomaszewska et al. 2013).

### **2.8.11. Fourier Transform Infrared Spectrometer (FTIR)**

Fourier transform infrared spectroscopy measure the reflectance and transmittance of a species to identify its chemical structure. It can give both qualitatively and quantitatively information by bombardment of infrared beam to the surface of the sample. The measurements can be made solid and liquid samples. To get more intense signals, the attenuated total reflectance (ATR) apparatus can be used, ATR can be made with ZnSe, diamond, Ge or Si (Madejová 2003).

## CHAPTER 3

### RESULTS AND DISCUSSION

#### 3.1. Hydrogeochemical Properties of Geothermal Fluids

Sodium and chloride are the dominant ions in the geothermal fluids of the TGF. The reddish-black color of the geothermal brine, which has high  $Mg^{2+}$ ,  $Ca^{2+}$ ,  $K^+$ , and  $Fe^{2+}$  contents, is attributed to the dissolution of ferromagnesian minerals present within Miocene volcanic rocks, which consist of trachyte, andesite, and trachyte-andesite (see Figure 3.1). These rocks are highly altered and contain quartz, K-feldspar, biotite, amphibole, sanidine, chalcopyrite, pyrite, and hematite. The concentrations of ions such as  $Li^+$ ,  $B^{3+}$ , and  $Sr^+$  in geothermal fluids were found to be extremely high in the TGF and have been observed to reach 20, 25, and 180 mg/L, respectively (Figure 3.1). This is related to the presence of volcanic rocks but may also be controlled by the degassing of magma intrusions (Baba et al., 2015).

Figure 3.2 and 3.3 show the saturation indices (SIs) of relevant hydrothermal minerals as a function of temperature for the TGF. The SIs were initially calculated using PHREEQCI computer code (Parkhurst and Appelo, 1999) at the outlet temperature and measured pH value. The SI is used to assess the departure of mineral saturation from equilibrium and is expressed as  $SI = (\log Q)/K$ , where  $Q$  is the reaction quotient/activity product of the mineral dissolution reaction and  $K$  is the equilibrium constant. The SIs with respect to chalcedony and quartz approached zero at  $\sim 200$  °C in samples from production wells T9 and T16 collected in March 2015 (Figure 3.2a and 3.3a). There is a significant correlation between the formation of chalcedony and/or saturation of quartz and the temperature. The calculated SIs of chalcedony and quartz increased with decreases in the calculated temperature. The SIs of other saturation minerals such as chrysotile, talc, sepiolite, willemite, and  $Pb(OH)_2$  increased with increases in the calculated temperature (Figure 3.2b and 3.3b).

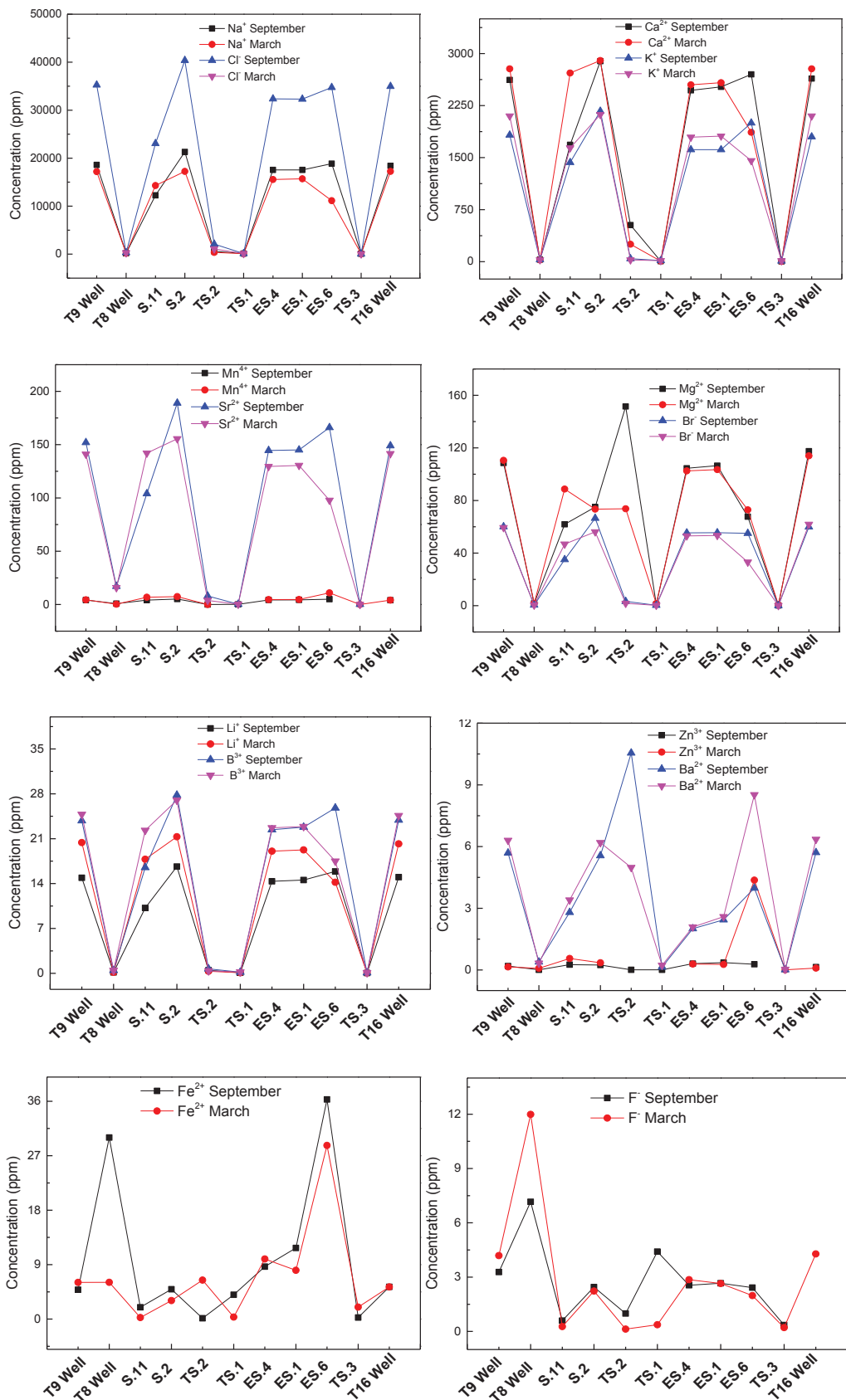


Figure 3.1. Major ions and heavy metals in Tuzla Geothermal Fluid.

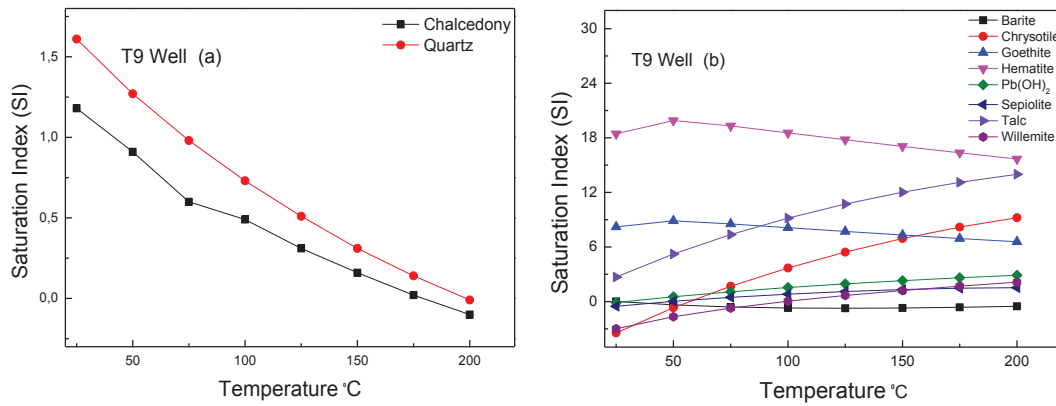


Figure 3.2. Scaling potential of Tuzla Geothermal Field production wells (T9) upon boiling of aquifer fluid a) Silicate, b) Potential deposits.

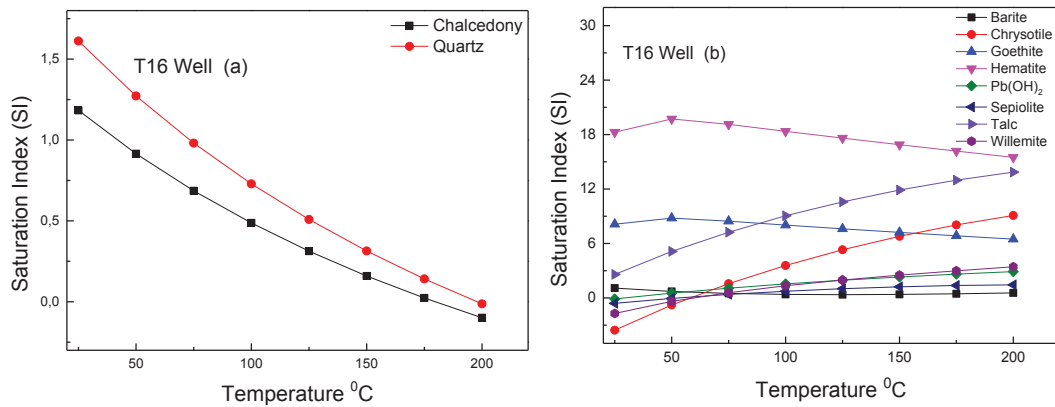


Figure 3.3. Scaling potential of Tuzla Geothermal Field production wells (T16) upon boiling of aquifer fluid a) Silicate, b) potential deposits.

### 3.2. Morphology and Structure of the Deposits

The quantitative properties of TGF fluids and deposits have been investigated, in which the concentrations of ions in decantates and the elemental mass compositions (%) of TGF deposits were reported by Dogan et al. (2014). The results show that the deposit observed in the pipeline is (Fe, Mg) silicate. On the other hand, the brine was found to contain a very high concentration of NaCl, and its electrical conductivity was measured to be 100 mS/cm, which is almost double that of seawater. The morphology of deposits was examined using SEM. Figure 3.4 shows representative SEM micrographs of natural deposits from the TGF and synthetic deposits obtained using reflux and autoclave techniques. Natural TGF deposits are heterogeneous in nature (Figure 3.4a) and contain spherical components with a size of less than 1  $\mu\text{m}$ . This feature may be associated with

the presence of amorphous silica, which is considered to be one of the main components of the deposit. The submicron size allows agglomeration into larger structures to occur such that only part of an agglomerate is observed in the field of an electron micrograph. In addition, although this may not be clearly seen in the SEM image, a controlled spherical aggregate of sharp flakes is present, as was shown in our previous study (Demir et al., 2014). This structure can be attributed to the formation of a double layer, which presumably consisted of  $\text{Fe}^{2+}$  and  $\text{Mg}^{2+}$  ions. These cations form positively charged layers separated by a distance of several angstroms with negatively charged ions, such as hydroxide, located in the intermediate region (Uan et al., 2010). The synthetic deposit prepared by refluxing exhibited a large feature in which nano sized spherical particles were hardly observed under  $\times 25000$  magnification (Figure 3.4b). Attempts to obtain higher-magnification images were unsuccessful owing to charging of the specimen. The reason for the formation of such a large agglomerate could be the low temperature employed during the synthesis of the deposit. On the other hand, the deposit prepared by autoclaving displayed a spherical morphology (Figure 3.4c) that was similar in size and shape to that found in the natural deposit.

Figure 3.5 presents the XRD patterns obtained from the three deposits. The diffraction patterns of all three samples suggest the presence of an amorphous material, which is indicated by the broad background. The reflections present within this amorphous background show the presence of  $\text{Fe}_3\text{O}_4$  (magnetite [ $\text{FeO}\cdot\text{Fe}_2\text{O}_3$ ], ICSD collection code 082446) in the natural (TGF) and autoclave deposits (Trial 6). The pattern of the autoclave deposit also shows the presence of  $\text{NaCl}$  (halite, ICSD collection code 041411) crystals. A similarity between the diffraction patterns of natural and autoclave deposits has also been reported in a previous study. The pattern of the deposit obtained by refluxing (Trials A, B, and C) indicates the presence of calcite magnesian mineral (ICSD collection code 040108). Those deposits are beyond the scope of this study. On the basis of the results obtained for the morphology and crystal structure, it can be concluded that the precipitates obtained from the autoclave reactor (in particular Trial F) have similar features to the deposit obtained from the vaporizer of the TGPP.

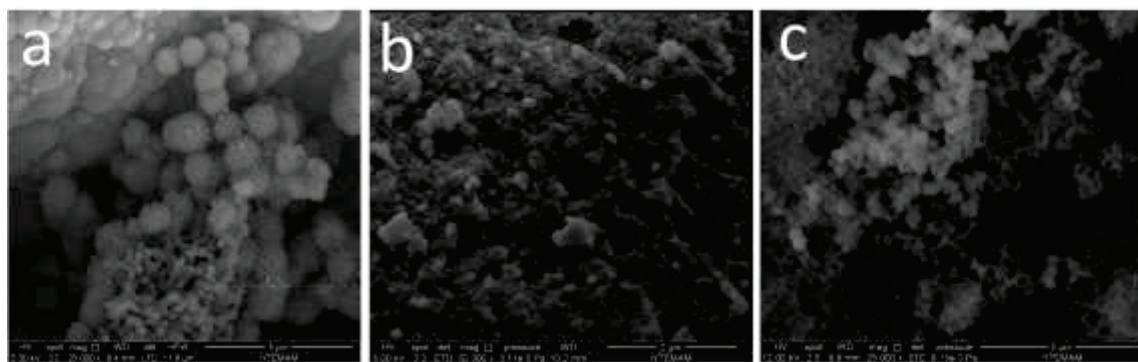


Figure 3.4. SEM images of deposits obtained from a) TGF (vaporizer)  $\times 25k$ , b) Reflux  $\times 50k$ , and c) Autoclave  $\times 25k$ .

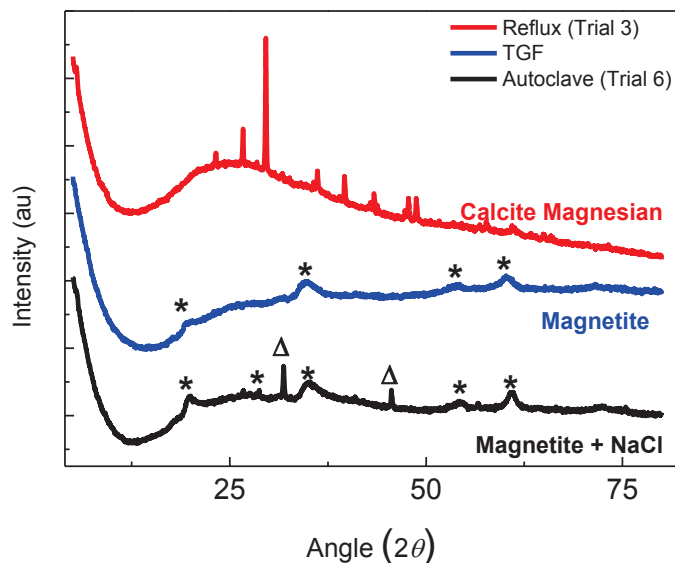


Figure 3.5. XRD of deposits obtained from TGF (vaporizer), Reflux, and Autoclave (Magnetite \*, NaCl Δ).

### 3.3. Spectroscopic Characterization of the Deposits

The chemical composition of the artificial and naturally formed deposits is reported in Table 3.1., which shows that the materials consist of a mixture of Si, Fe, Mg, Na, and Ca. The samples were evaluated using spectroscopic analytical methods to obtain an insight into their structural formation.

Table 3.1. Mass percent composition of deposits obtained from Reflux and Autoclave. TGF results are based on the previous study (Source: Dogan et al., 2014).

System	Fe	Mg	Ca	Na	SiO <sub>2</sub>
Reflux (Trial C)	13	3	7	4	51
Autoclave (Trial F)	16±2	4±1	3±1	3±2	50±3
Natural (Dogan et al. 2014)	17	4	2	1	38

The presence of iron species in the precipitates enables EPR to be used for the appropriate measurements (Weckhuysen, Heidler, and Schoonheydt 2004). In general, Fe<sup>3+</sup> ions ( $d^5, S = 5/2$ ) are in a high-spin electronic configuration in the presence of weak field ligands such as oxygen, water, or hydroxyl ligands (Goldfarb et al. 1994). Furthermore, according to their chemical environment, Fe<sup>3+</sup> species generate EPR signals with different *g* values. The usual X-band EPR signals of Fe<sup>3+</sup> are observed at  $g \approx 4.2$ – $4.3$ ,  $g \approx 2.2$ , and  $g \approx 2.0$  (Kim et al. 2010). Although alternative interpretations exist in the literature for the assignments of these EPR signals, the commonly accepted assignments are as follows: framework iron in a tetrahedral environment and iron oxide species and iron ions coupled by exchange interactions in a distorted octahedral environment, respectively (Srinivasulu et al. 2013, Weckhuysen, Heidler, and Schoonheydt 2004).

Figure 3.6a shows the X-band EPR spectra of TGF and artificial deposits (Trial E and Trial G, latter deposit containing no iron), which were recorded at room temperature. The spectra of the TGF deposit and the artificial precipitate from Trial E were normalized to the same iron content. The same amount of precipitate without iron (Trial G), which was also measured as a reference sample, displayed two weak signals at  $g = 4.2$  and  $g = 2.0$  owing to trace amounts of iron, whereas the remaining components of the precipitates did not contribute to the EPR spectrum. The TGF and Trial E deposits exhibited two signals: an intense signal at  $g = 2.2$  and a weak signal at  $g \approx 4.2$ . The intense signal observed at  $g = 2.2$  shows the formation of iron oxide clusters in both TGF and artificial (Trial E) deposits. The weak signal at  $g \approx 4.2$  indicates the presence of substituted Fe<sup>3+</sup> ions in the framework of both the TGF deposit and the artificial (Trial E) precipitate.

Ferrous chloride can be oxidized to ferric chloride in the reaction medium (air and water vapor). Nevertheless, the results for both the TGF deposits and the synthetic precipitates indicate the coexistence of ferric and ferrous ions. These results suggest that the presence of air in the reaction medium was not able to oxidize the entire ferrous ion content. Note that the presence of ferric ions gives rise to magnetic behavior. Both the natural deposit and the autoclave precipitate displayed magnetic behavior, which also confirms the presence of both ions and rules out the complete oxidation of ferrous ions to ferric ions.

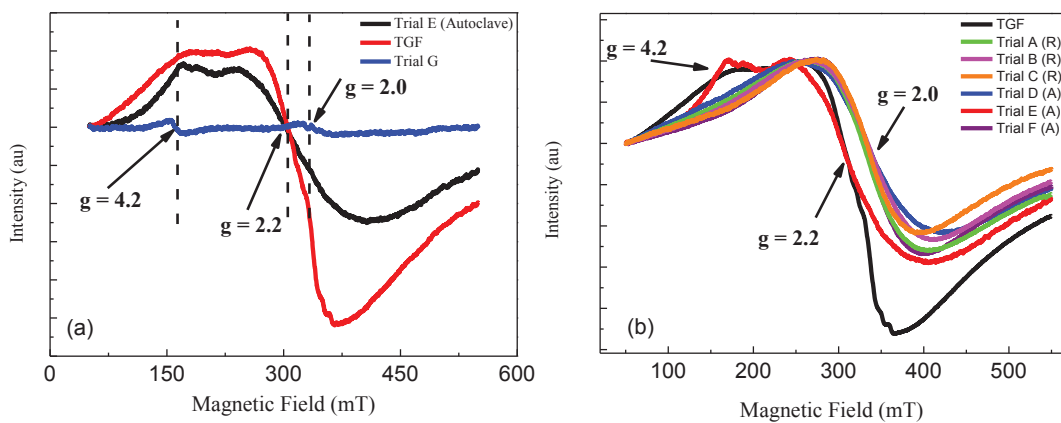


Figure 3.6. X-band EPR spectra of TGF and artificial deposits (Trial E, and Trial G, latter deposit containing no iron) recorded at room temperature. The spectra of TGF deposit and artificial Trial E sample were normalized to the same iron content (a), X-band EPR spectra of TGF and artificial deposits (Trial A, B, C, D, E and F) recorded at room temperature. The spectra were normalized to their maxima (b).

The EPR spectra recorded for the other precipitates (Trials A, B, C, D, and F) show the appearance of a new broad signal at  $g \approx 2.0$ , whereas the signals at  $g = 4.2$  and  $g \approx 2.2$ , which were observed for the natural and artificial Trial E samples, have disappeared (Figure 3.6b). In the literature, intense EPR signals at  $g \approx 2.0$  have been attributed to the formation of iron clusters by spin-spin interactions and to iron ions coupled by exchange interactions in a distorted octahedral environment (Muralidhara et al. 2010). Although the  $g$  values of the TGF deposit are similar to those of the artificial Trial 5 precipitate, they are different from the  $g$  values of the other artificial precipitates (Trials A, B, C, D, and F in Figure 3.6b). These results provide an understanding of the chemical environment and structure of iron species in the artificial precipitates based on their method of preparation and their initial compositions.

XPS was employed to investigate the compositions of the samples. The binding energies of atoms give information about the structure of materials. Figure 3.7 shows the XPS survey spectra of the natural (TGF) deposit and an artificial precipitate obtained using the autoclave system (Trial F). Both spectra show an intense oxygen (O 1s) signal and weaker signals of Mg 1s, Fe 2p, Fe 3p, Si 2p, Ca 2p, and Na 1s. The peak binding energies for each of these signals are summarized in Table 3.2. The table also contains reference data for the binding energies of metals and oxygen obtained from the literature. The spectra (Figure 3.7b) show that the O 1s binding energies of the TGF deposit and autoclave precipitate were located at 532.0 and 532.7 eV, respectively (see also Table 3.2). Jensen et al. (2013) attributed a signal at 532.8 eV to what they referred to as lattice oxygens in  $\text{SiO}_2$ , where all four oxygen atoms are linked to silicon atoms (also referred to as bridging oxygens). When compared with the reference binding energy of 532.8 eV found by Jensen et al. (2013), the lower value found for the TGF deposit can be attributed to the presence of non-linked oxygens (also referred to as non-bridging oxygens) in the  $\text{SiO}_2$  framework (Mekki et al. 1996). The charge balance of the dangling bonds from the non-bridging oxygens is satisfied by the presence of metal cations (Mekki et al. 1996). The results also show that the O 1s binding energies of the autoclave precipitates exhibit much smaller differences, which suggests that these samples have lower amounts of non-bridging oxygens, i.e., they have more Si-O linkages. This finding may be associated with the absence of metal salts in the silicate networks of the autoclave precipitates in comparison with the TGF deposit. The reference binding energy of Si 2p (Figure 3.7b) at 103.5 eV is attributed to silicon atoms linked to oxygen atoms in the  $\text{SiO}_2$  tetrahedra (Mekki et al. 1996). In relation to the linked silicon atoms, a lower binding energy of 102.7 eV was measured for the TGF deposit, whereas the binding energy measured for the autoclave deposits was 103.5 eV, which was similar to the reference value. The lower binding energy in the TGF sample is explained by the relative lack of Si-O linkages in the  $\text{SiO}_2$  tetrahedra, where the metal ions have penetrated into the silica framework (Mekki et al. 1996). The kinetics of precipitate formation is very rapid in an autoclave in comparison to the formation of natural deposits in the TGF. Not surprisingly, the kinetics of deposit formation is very rapid in geothermal fields. Because the brine is pumped to the ground surface rapidly, the atoms do not have enough time to rearrange and form linkages, as they would in an equilibrium process. The lower binding energy in the TGF deposits is also consistent with the explanation of the difference in the O 1s binding energies between the two deposits. The TGF and autoclave deposits displayed Na 1s

signals at 1072.5 and 1072.9 eV, respectively. Normally, the Na 1s binding energy is 1071.5 eV (Mekki et al. 1996). The increase in the binding energy of Na atoms may be related to the binding of the atoms to other ionic atoms and hence to the presence of NaCl crystals. Similarly, the increase found in the binding energy of Ca 2p with respect to its reference value (see Table 3.2) may be associated with the formation of a crystalline calcium salt in both the TGF and autoclave deposits. The relatively higher binding energy associated with the TGF sample suggests that the concentration of such salts was higher in comparison with that in the autoclave sample. The similarity in the binding energies of Mg 1s suggests that the structural differences were slight, in particular between the TGF and autoclave deposits. The reference binding energies of Fe 2p and Fe 3p have been measured to be 711.0 and 55.6 eV, respectively. These reference values correspond to hematite ( $\text{Fe}_2\text{O}_3$ , Fe 2p) and magnetite ( $\text{Fe}_3\text{O}_4$ , Fe 3p) (Yamashita and Hayes 2008). The TGF and autoclave deposits displayed larger binding energy values for both iron compounds, as shown in Table 3.2. The results of XRD and EPR studies suggest that iron exists both in the form of magnetite crystals and dissolved as iron clusters within the amorphous silicate network. The XPS binding energy data for iron atoms do not appear to fully match those of magnetite crystals or show clear indications of an amorphous structure, which suggests that the XPS analysis was not able to clearly differentiate the different structures adopted by iron in the deposit.

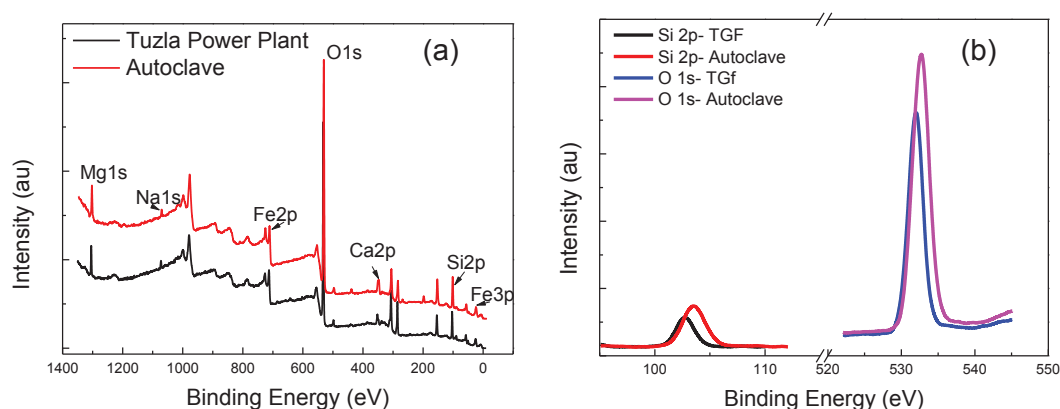


Figure 3.7. XPS survey spectra of the natural deposit and precipitate obtained from Autoclave system (a) overall, (b) Si 2p and O 1s atoms binding energy.

Table 3.2. Binding energies, in eV, for TGF and Autoclave samples, and reference compounds of identified metal salts.

<b>Binding Atom</b>	<b>TGF</b>	<b>Autoclave (Trial F)</b>	<b>Reference Compounds</b>
<b>O 1s</b>	532.0	532.7	532.8 ( $\text{SiO}_2$ ) (Jensen et al. 2013)
<b>Si 2p</b>	102.7	103.5	103.5 ( $\text{SiO}_2$ ) (Jensen et al. 2013)
<b>Na 1s</b>	072.5	1072.9	1071.5 ( $\text{Na}_2\text{O}$ ) (Mekki et al. 1996)
<b>Fe 2p</b>	712.1	712.8	711.0 ( $\text{Fe}_3\text{O}_4$ ) (Yamashita and Hayes 2008)
<b>Fe 3p</b>	56.6	57.8	55.6 ( $\text{Fe}_2\text{O}_3$ ) (Yamashita and Hayes 2008)
<b>Mg 1s</b>	304.2	1304.6	1304.5 ( $\text{MgO}$ ) ( <a href="http://xpssimplified.com/elements/magnesium.php">http://xpssimplified.com/elements/magnesium.php</a> 28.01.2017)
<b>Ca 2p</b>	351.7	348.6	347.2 ( $\text{CaCO}_3$ ) ( <a href="http://xpssimplified.com/elements/calcium.php">http://xpssimplified.com/elements/calcium.php</a> 28.01.2017)

### 3.4. Effect of Metal Cations

To get an insight into the association of metal cations with silicates, the same reaction (under the conditions used in Trial F) was performed in the absence of each cation ( $\text{Fe}^{2+}$ ,  $\text{Mg}^{2+}$ , and  $\text{Ca}^{2+}$  in Trial G, H, and J, respectively) (Table 2.1). In the presence of 2 g/L  $\text{SiO}_2$ , each cation was removed from the composition consecutively and the resulting deposit was examined by XRD. Figure 3.8 presents the XRD patterns of the samples obtained from these reactions. Trials H and J (in the absence of calcium and magnesium, respectively) provided amorphous patterns, whereas the absence of iron yielded a crystalline pattern (Trial G) that matched that of the calcite form of  $\text{CaCO}_3$  for a product in the form of a soft, white powder. This result highlights the importance of the presence

of iron in the chemical composition of the deposit and suggests that iron has a stronger tendency to become incorporated in the silicate structure in comparison to  $\text{Ca}^{2+}$  and  $\text{Mg}^{2+}$ , which prevents the formation of  $\text{CaCO}_3$ . This result is corroborated by the EPR measurements.

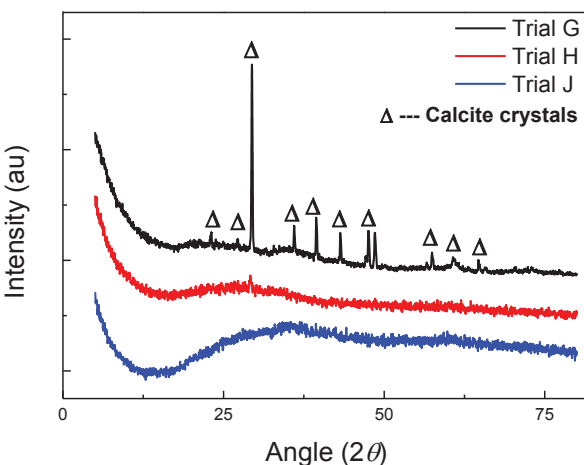


Figure 3.8. XRD pattern of the deposits obtained from Na Silicate in the presence of various salts given in Table 2.1 (Trial G ( $\text{Na}^+$ ,  $\text{Ca}^{2+}$ ,  $\text{Mg}^{2+}$  and  $\text{SiO}_2$ ), Trial H ( $\text{Na}^+$ ,  $\text{Ca}^{2+}$ ,  $\text{Fe}^{2+}$  and  $\text{SiO}_2$ ) and Trial J ( $\text{Na}^+$ ,  $\text{Mg}^{2+}$ ,  $\text{Fe}^{2+}$  and  $\text{SiO}_2$ ).

### 3.5. Inhibition of Scale by Polymeric Compounds

The inhibition performances of water soluble polymeric molecules were tested by monitoring the concentration of soluble silicic acid in the leftover solution. 200 mL of artificial brine solution, that has already been investigated and composed of chlorine salts of iron, magnesium and calcium, and sodium silicate and sodium carbonate, was maintained to the autoclave reactor system. Initial pressure and temperature values were 1 bar and room temperature, respectively. Solution was reacted till reaching 3.2 bar pressure and 137.6 °C temperature values. The reacting mixture was then collected in a plastic bottle to shock in an ice-water bath. 50 mL of inhibitor solution was added at elevated dosage levels to the reacting mixture as soon as possible. Scaling occurred at this stage for this reason metal-silicate scaling should be inhibited. Sudden decrease in temperature and pressure causes uncontrolled and amorphous structure of metal-silicate precipitation, because solubility is a function of temperature. Decrease in solubility occurs the same as in geothermal power plants. So, the injection of antiscalant molecule should be done as soon as possible.

Acrylamide, vinyl sulfonic acid sodium salt and vinyl phosphonic acid monomers were polymerized to homopolymers (PVSA, PVPA and PAM), copolymers (PAM-co-VSA, PAM-co-VPA and PVSA-co-VPA) and terpolymers (PAM-co-VSA-co-VPA). The molecular weights of each polymer were investigated and monomer compositions of copolymer and terpolymer calculated which are represented in Table 3.3.

Each polymer was tested at various dosage levels (25, 50 and 100 ppm). Soluble silica,  $Mg^{2+}$  and  $Fe^{2+}$  concentrations were monitored for each trial and represented in Figure 3.9. The dashed lines in Figure 3.9a, b and c demonstrates the concentrations of each components that was measured in the absence of inhibitor solution (Trial F). According to the results, soluble silica concentration for all antiscalant molecules are higher than the artificial brine solution which means the synthesized inhibitors are promising for the mitigation of metal-silicate scaling. XRD, XPS, XRF and EPR results are correlated and showed that oxide forms of magnesium and iron are formed and penetrated in to the amorphous silica network. For this reason, soluble  $SiO_2$ ,  $Mg^{2+}$  and  $Fe^{2+}$  concentrations are investigated separately in Figure 3.9 a, b and c, respectively. To understand this relation, chelation abilities of polymers with metal cations were examined with FTIR spectroscopy technique. They were tested for both in scale and their solutions with metal cations.

In Figure 3.9a the concentration of soluble silicic acid increases with increasing dosages of PAM and PVPA, but maximum silica concentration is observed with PVSA molecule. Maximum soluble silicic acid concentration for PAM, PVSA and PVPA molecules are 188, 221 and 180 ppm, respectively. Although PVSA gives the best result, its inhibition performance decreases with increasing dosage level. The reason may be the formation of flocculation of the  $SiO_2$  with PVSA molecules. Fortunately, the silica concentration is higher than the solubility limit of silica which was measured for Trial F. Soluble silica concentrations of PAM-co-VSA increases with increasing dosage. Above 50 ppm dosage level solubility is higher than solubility limit of silica and reaches up to 195 ppm  $SiO_2$ . In contrast to PAM-co-VSA molecule, soluble silicic acid concentration decreases with increasing dosage of PAM-co-VPA molecule. Among these three copolymers, PVSA-co-VPA molecule shows the best inhibition performance and promising up to 50 ppm dosage level. The solubility level increases from 134 ppm to 225 ppm. The combination of three homopolymers' (PAM-co-VSA-co-VPA tercopolymer) antiscalant performance is promising, but soluble silicic acid concentration nearly the same for all dosage levels (around 190 ppm). The efficacies of all polymers are calculated according to Equation 2.1. Maximum inhibition performance is observed with PVSA-co-

VPA molecule with 50 ppm dosage (34%) and PVSA molecule follows with 25 ppm dosage (33%).

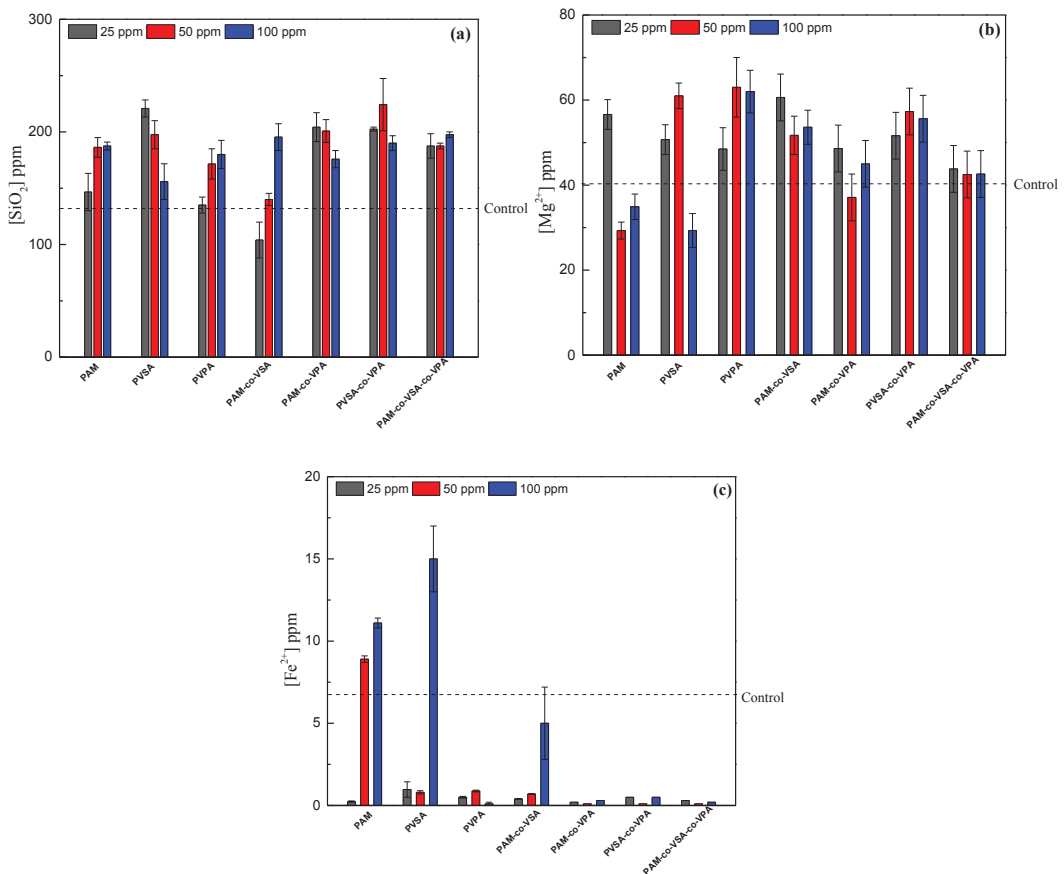


Figure 3.9. Solubility profiles of (a) SiO<sub>2</sub>, (b) Mg<sup>2+</sup>, (c) Fe<sup>2+</sup> in the presence of various inhibitors at different dosages. Dashed line refers to the control sample.

Soluble silicic acid concentration is decreasing with increasing water hardness. To investigate the inhibition efficiency of magnesium ion with these antiscalant molecules, concentrations of Mg<sup>2+</sup> and Fe<sup>2+</sup> (iron precipitates and found in both natural and artificial deposits) was monitored. Magnesium concentration decreases in the presence of PAM molecule. According to the results in Figure 3.9b, Mg<sup>2+</sup> level decreases with increasing dosage of PAM and has below the solubility limit of magnesium in Trial F. Moreover, same result observed with PAM-co-VPA molecule. Concentration of magnesium ion in decantates is higher than the solubility limit which is referred with dashed lines, for PVSA (50 ppm), PVPA (50 ppm), PAM-co-VSA (25 ppm) and PVSA-co-VPA (50 ppm). Soluble magnesium concentration in decantate in the same level of solubility limit for PAM-co-VSA-co-VPA molecule. Maximum level of Mg<sup>2+</sup>

concentration is observed by using PVPA and; PAM-co-VSA for 50 and 25 ppm dosages, respectively. In Figure 3.9c, concentration of iron is represented. According to the results,  $\text{Fe}^{2+}$  is least abundant in decantate, which means iron precipitates most with  $\text{SiO}_2$  thus, XRD results show broad magnetite mineral's signals that placed in to the amorphous silica network. None of the anti scalants isn't promising and iron concentration is found lower than limit of  $\text{Fe}^{2+}$ . This result can be explained with the competence of the cations that give precipitation reaction with silica. Because of chelation between magnesium ion and polymer molecule may resulted as more  $\text{Fe}^{2+}$  precipitation (Topçu et al. 2017).

The inhibition efficiency of any antiscalant molecule was performed in literature with only 500 ppm of  $\text{SiO}_2$  solution (Demadis and Neofotistou 2004, Demadis et al. 2005, Demadis and Stathouloupolou 2006, Gallup 2002, Gallup et al. 2003). In this case, the mixture of metal cations and  $\text{Na}_2\text{SiO}_3$  solutions were tested.

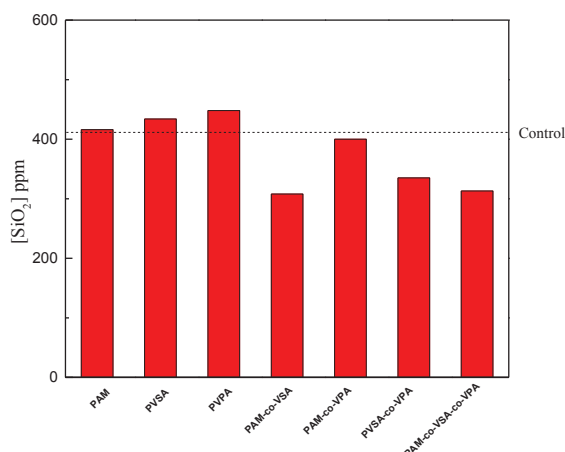


Figure 3.10. Soluble  $\text{SiO}_2$  concentration in the various antiscalants. Only Na-Silicate is used as reactant without having metal salts. For each polymer, most effective dosage in brine trials was used. (PAM: 100 ppm, PVSA:25 ppm, PVPA: 100 ppm, PAM-co-VSA:100 ppm, PAM-co-VPA: 25 ppm, PVSA-co-VPA: 50 ppm, PAM-co-VSA-co-VPA: 100 ppm.)

To understand the relation between inhibitor molecule and  $\text{SiO}_2$ ,  $\text{Mg}^{2+}$  and  $\text{Fe}^{2+}$ , each of polymer solutions were tested with 2000 ppm  $\text{SiO}_2$  solution. Soluble silicic acid concentration reacted in autoclave without any metal cations is 408 ppm. In Figure 3.10 each of antiscalant molecule were tested and their results are represented. Each trial performed with only 200 mL of 2000 ppm  $\text{SiO}_2$  solutions. According to the results, soluble silicic acid concentrations are close to the solubility limit of  $\text{SiO}_2$  (dashed lines refer as 408 ppm). Moreover, antiscalant molecules that were tested, have chelation

ability with metal cations. This result proved with FTIR studies. Interactions between pendant groups on polymeric molecules and metal ions were investigated and results are represented in Figure 3.11 and Table 3.4. this result may be explained with the electrostatic interactions between negatively charged active groups on polymers and negatively charged silica particles and positively charged metal ions. Because of repulsive and attractive forces, polymers interact with metal cations and they have promising efficiency for metal-silicate scaling.

**Table 3.3. Molecular properties and efficiency of silicate solubility of the co/polymers.**

	M <sub>w</sub> kDa	Feed composition <i>mol:mol</i>	Composition of the backbone <i>mol:mol</i>	Dosage ppm	Silica Inhibition Efficiency %
PAM	43.1	1	1	25	4.8
				50	19.5
				100	20.3
PVSA	48.1	1	1	25	32.7
				50	24
				100	8.2
PVPA	22.7	1	1	25	0.3
				50	14.2
				100	17.2
P(AM-co-VSA)	85.4	1:1	0.5:0.5	25	-11.2
				50	2.2
				100	22.9
P(VSA-co-VPA)	78.7	1:1	0.2:0.8	25	21
				50	33.8
				100	25.5
P(AM-co-VPA)	23.6	1:1	0.7:0.3	25	26.3
				50	25.1
				100	15.7
P(AM-co-VSA-co-VPA)	51.5	1:1:1	0.25:0.25:0.5	25	23.6
				50	19.9
				100	19.9

To clarify the interaction between the monomeric species and metal cations, each salt ( $\text{CaCl}_2$ ,  $\text{MgCl}_2$  and  $\text{FeCl}_2$ ) was treated with the antiscalant polymers (1:1) separately. The resulting solutions were subjected to FTIR spectroscopy. The spectra are given in Figure 3.11. The vibrational signal and its shifting in the presence of the metal cations are shown in Table 3.4. For amide, there are 3 possible bands that can act as a ligand, which

are amide I, II and III appearing at  $1650\text{ cm}^{-1}$ ,  $1452\text{ cm}^{-1}$  and  $1350\text{ cm}^{-1}$ , respectively. The shifting of wavenumber for amide I appears nearly  $20\text{ cm}^{-1}$ . It is about  $4\text{ cm}^{-1}$  for amide II and III bands. Similarly, the stretching of S-O bond in sulfonic acid is also affected in the presence of metal cation. The  $1162\text{ cm}^{-1}$  stretching vibrational signal of sulfonic acid is shifted to higher wavenumbers indicating the existence of interaction. Both amide (I, II, III) and S-O stretching bands appeared high energetic while these bands were treated with metals. For phosphonic acid, the interaction with metals may occur on oxygen of P-OH, and this interaction cause to shifting on stretching band at  $1164\text{ cm}^{-1}$ . Unlike the other groups, phosphonic acid was shifted only by treatment with calcium salt. The length of the P-O bond extended in the interaction with calcium, so that the peak of this bond shifted towards the low-energy region. It can be concluded that, amide and sulfonic acid groups interact particularly with both  $\text{Fe}^{2+}$  and  $\text{Mg}^{2+}$ , while phosphonic acid groups have tendency to interact only with  $\text{Ca}^{2+}$ .

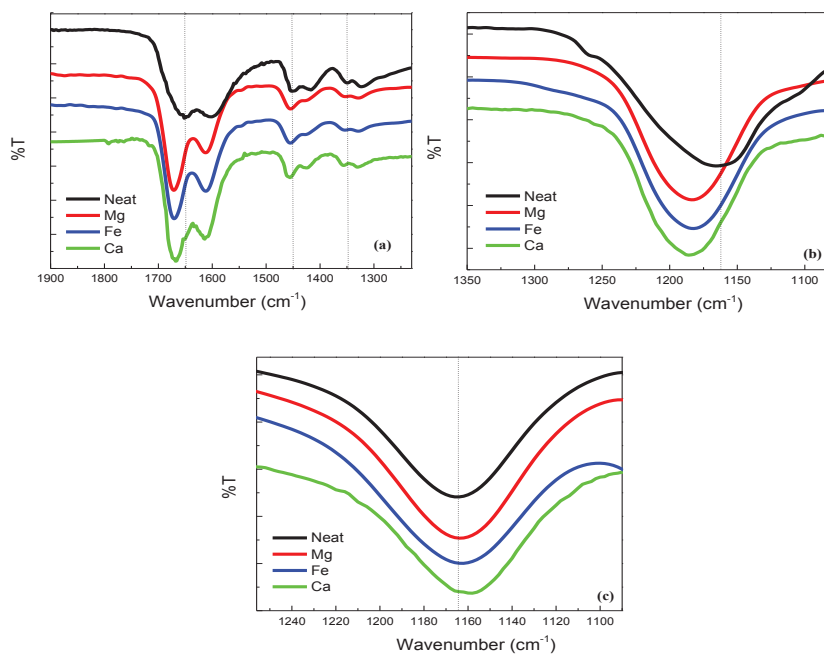


Figure 3.11. FTIR spectrum of pendant group of (a) PAM, (b) PVSA and (c) PVPA with metals (Ca, Mg, Fe), that possibly act as a ligand.

Table 3.4. Characteristic absorption bands in the IR spectra of the polymers (PAM, PVSA, and PVPA) and their metal complexes ( $\nu$ ,  $\text{cm}^{-1}$ ), (resolution:  $2 \text{ cm}^{-1}$ ).

		+CaCl <sub>2</sub>	+FeCl <sub>2</sub>	+MgCl <sub>2</sub>
	Neat polymer	$\Delta\nu$		
Amide I band (PAM)	1652	+18	+20	+22
Amide II band (PAM)	1452	+4	+4	+2
Amide III band (PAM)	1350	+6	+4	+4
S-O stretching (PVSA)	1162	+10	+6	+8
P-O stretching (PVPA)	1164	-6	0	0

The formation of silicate scale is based on the condensation reactions between the silicic acid molecules. Silica particles are soluble till they form tetramers of silicic acids. In the first stage, tetramers are formed and they come together in cyclic forms. Agglomeration continues and new clusters precipitates after they reach to a critical nucleus. These processes occur uncontrolled because of sudden decrease in temperature and amorphous nature of the silica precipitation. The procedures to minimize silicate scaling can be with two different mechanism. First one is mitigation of metal cations that catalyze the silica precipitation with chelation ability of an inhibitor molecule, and, another route may be the dispersion of silica particles with a proper colloid molecule. The synthesized molecules are available for the mitigation mechanism and the results are encouraging for the minimization of metal-silicate scaling studies. The highest efficiency was observed with PVSA-co-VPA molecule, which is applied 50 ppm optimum dosage.

Increasing dosage level has detrimental effect on inhibition activity. The reason may be explained with flocculation mechanism. The schematic representation is given in Figure 3.12.

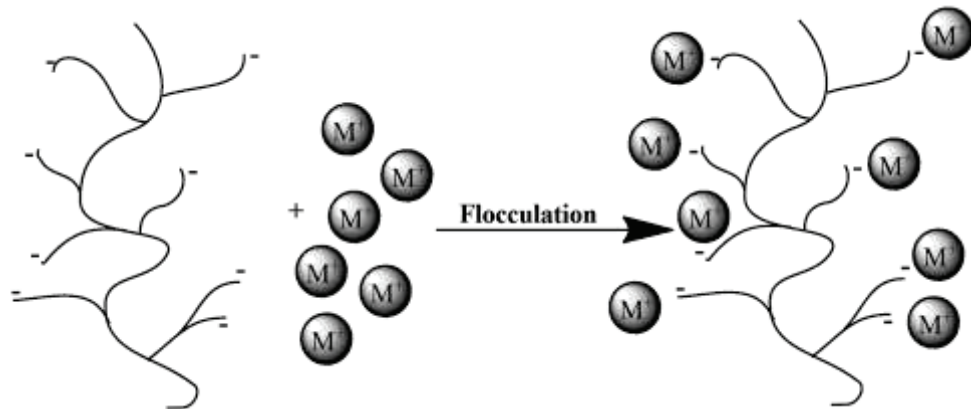


Figure 3.12. Schematic representation of flocculation mechanism in the presence of metal cations and negatively charged polymer.

The reason of decrease in inhibition performance with increasing molecular weight of polymers may be the flocculation mechanism between negatively charged polymers and positively charged metal cations.

## CHAPTER 4

### CONCLUSION

Tuzla geothermal brine is hypersaline and causes the formation of deposits with various chemical compositions. The chemical compositions of these deposits, for instance, quartz and chalcedony, were estimated from SIs using PHREEQCI computer code. The results were consistent with those for natural deposits observed in the field that have been indexed as magnetite in an amorphous silicate network. A reflux system, which is commonly employed in many chemistry laboratories, was used for the synthesis of artificial deposits. An alternative strategy was developed for the synthesis of artificial deposits using an autoclave reactor, in which conditions in the field can be replicated. Examinations of the morphology and structure of the deposits (both naturally formed and artificially generated) are in agreement with the estimates made using the computer code. In contrast to those produced by the reflux system, the artificially generated deposits obtained using the autoclave reactor were found to be similar to the naturally formed deposits in terms of their internal structure and elemental composition. The microscopic and spectroscopic analytical techniques used in the study were shown to be effective in determining the nature of the natural and artificially formed samples. Analysis by electron microscopy revealed that the morphology of the natural deposits and samples formed in the autoclave mainly comprised clusters of nanoscale particles that had a spherical geometry. Via XRD, EPR, and XPS examinations, the structures of these formations were found to contain both crystalline and amorphous regions. The crystalline region was identified as consisting of magnetite ( $\text{Fe}_3\text{O}_4$ ) and salts of sodium, calcium, and magnesium. The amorphous portion was identified as a silicate structure modified by sodium, iron, and calcium. The methodology and findings used in this study show that this strategy can be employed in the laboratory to test the performance of potential inhibitors. Furthermore, the structural and morphological information obtained from the precipitates can be utilized in designing efficient inhibitors of metal silicate deposits.

Homopolymer, co-polymer and terco-polymer of AM, VSA-sodium salt and VPA's inhibition performances were represented, which were synthesized by free radical addition polymerization. The antiscalant molecules were tested in autoclave system in which the conditions were obtained very close to that observed in the field. The efficacies

were calculated according to soluble silicic acid concentrations that measured after isolation the precipitate from decantate. The macromolecules used in this work are potential antiscalant, because their inhibition mechanism seems to be as chelation with metal cations. This hypothesis was proved with FTIR studies. Moreover, the catalytic effect of metal cations was measured.  $\text{SiO}_2$  precipitated more with calcium than tested and according to the results soluble silicic acid concentration is in highest level in the absence of  $\text{Ca}^{2+}$ . All in all, VPA is more associated with  $\text{Ca}^{2+}$ , VSA can be interacted with soluble silicic acid via electrostatic interactions.

## REFERENCES

- Amjad, Zahid, and Konstantinos D Demadis. 2015. *Mineral Scales and Deposits: Scientific and Technological Approaches*: Elsevier.
- Baba, Alper, Mustafa M Demir, Gonca A Koç, and Celal Tuğcu. 2015. "Hydrogeological properties of hyper-saline geothermal brine and application of inhibiting siliceous scale via pH modification." *Geothermics* 53:406-412.
- Bernal, Juan Pablo, and Rufino Lozano-Santacruz. 2005. "Characterization of a new set of eight geochemical reference materials for XRF major and trace element analysis." *Revista Mexicana de Ciencias Geológicas* 22 (3):329-344.
- Bingöl, Bahar, Wolfgang H Meyer, Manfred Wagner, and Gerhard Wegner. 2006. "Synthesis, microstructure, and acidity of poly (vinylphosphonic acid)." *Macromolecular Rapid Communications* 27 (20):1719-1724.
- Brinker, C Jeffrey, and George W Scherer. 2013. *Sol-gel science: the physics and chemistry of sol-gel processing*: Academic press.
- Brown, Kevin. 2011. "Thermodynamics and kinetics of silica scaling." International Workshop on Mineral Scaling.
- Chastain, Jill, Roger C King, and JF Moulder. 1995. *Handbook of X-ray photoelectron spectroscopy: a reference book of standard spectra for identification and interpretation of XPS data*: Physical Electronics Eden Prairie, MN.
- Chauhan, Kalpana, Priyanka Patiyal, Ghanshyam S Chauhan, and Praveen Sharma. 2014. "Star-shaped polymers of bio-inspired algae core and poly (acrylamide) and poly (acrylic acid) as arms in dissolution of silica/silicate." *Water research* 56:225-233.
- Chen, Chen-Tung A, and William L Marshall. 1982. "Amorphous silica solubilities IV. Behavior in pure water and aqueous sodium chloride, sodium sulfate, magnesium chloride, and magnesium sulfate solutions up to 350 C." *Geochimica et Cosmochimica Acta* 46 (2):279-287.
- Clark, BJ, T Frost, and MA Russell. 1993. *UV Spectroscopy: Techniques, instrumentation and data handling*. Vol. 4: Springer Science & Business Media.
- Çelik, Aslı, Gökhan Topçu, Alper Baba, Yasar Akdogan, Ufuk Şentürk, and Mustafa M Demir. 2017. "Experimental modeling of silicate-based geothermal deposits." *Geothermics* 69:65-73.
- Demadis, Konstantinos D. 2012. "Catalytic Effect of Magnesium Ions on Silicic Acid Polycondensation and Inhibition Strategies Based on Chelation." *Industrial & engineering chemistry research* 51:9032-9040. doi: 10.1021/ie3010836 |

- Demadis, Konstantinos D, Eleftheria Mavredaki, Aggeliki Stathoulopoulou, Eleftheria Neofotistou, and Chris Mantzaridis. 2007. "Industrial water systems: problems, challenges and solutions for the process industries." *Desalination* 213 (1):38-46.
- Demadis, Konstantinos D, and Eleftheria Neofotistou. 2004. "Inhibition and growth control of colloidal silica: Designed chemical approaches." *Materials performance* 43 (4):38-42.
- Demadis, Konstantinos D, Eleftheria Neofotistou, Eleftheria Mavredaki, Michalis Tsiknakis, Eva-Maria Sarigiannidou, and Stella D Katarachia. 2005. "Inorganic foulants in membrane systems: chemical control strategies and the contribution of "green chemistry"." *Desalination* 179 (1):281-295.
- Demadis, Konstantinos D, and Aggeliki Stathoulopoulou. 2006. "Solubility enhancement of silicate with polyamine/polyammonium cationic macromolecules: relevance to silica-laden process waters." *Industrial & engineering chemistry research* 45 (12):4436-4440.
- Demir, Mustafa M, Alper Baba, Vedat Atilla, and Mustafa Inanlı. 2014. "Types of the scaling in hyper saline geothermal system in northwest Turkey." *Geothermics* 50:1-9.
- Dogan, Irmak, Mustafa M Demir, Alper Baba, A Baba, D Bundschuh, and D Chandrasekharam. 2014. "Scaling problem of the geothermal system in Turkey." *Geothermal Systems and Energy Resources, Turkey and Greece*:225-234.
- Ehrlich, Hermann, Konstantinos D Demadis, Oleg S Pokrovsky, and Petros G Koutsoukos. 2010. "Modern views on desilicification: biosilica and abiotic silica dissolution in natural and artificial environments." *Chemical Reviews* 110 (8):4656-4689.
- Gallup, Darrell L. 1997. "Aluminum silicate scale formation and inhibition: scale characterization and laboratory experiments." *Geothermics* 26 (4):483-499.
- Gallup, Darrell L. 1998. "Aluminum silicate scale formation and inhibition (2): scale solubilities and laboratory and field inhibition tests." *Geothermics* 27 (4):485-501.
- Gallup, Darrell L. 2002. "Investigations of organic inhibitors for silica scale control in geothermal brines." *Geothermics* 31 (4):415-430.
- Gallup, Darrell L, and Emy Barcelon. 2005. "Investigations of organic inhibitors for silica scale control from geothermal brines-II." *Geothermics* 34 (6):756-771.
- Gallup, Darrell L, Frankie Sugiaman, Vilma Capuno, and Alain Manceau. 2003. "Laboratory investigation of silica removal from geothermal brines to control silica scaling and produce usable silicates." *Applied Geochemistry* 18 (10):1597-1612.

- Ghouil, Boudjema, Abdelhamid Harabi, Ferhat Bouzerara, Boukhemis Boudaira, Abdelkrim Guechi, Mustafa M Demir, and Alberto Figoli. 2015. "Development and characterization of tubular composite ceramic membranes using natural alumino-silicates for microfiltration applications." *Materials Characterization* 103:18-27.
- Girma, KB, Volker Lorenz, Steffen Blaurock, and Frank T Edelmann. 2005. "Coordination chemistry of acrylamide." *Coordination Chemistry Reviews* 249 (11):1283-1293.
- Girma, KB, Volker Lorenz, Steffen Blaurock, and Frank T Edelmann. 2006. "Coordination chemistry of acrylamide 3: Synthesis, crystal structure and IR spectroscopic properties of dichloro-tetrakis (O-acrylamide) copper (II),[Cu (O-OC (NH<sub>2</sub>) CH]. *Inorganica chimica acta* 359 (1):364-368.
- Goldfarb, D, M Bernardo, KG Strohmaier, DEW Vaughan, and H Thomann. 1994. "Characterization of iron in zeolites by X-band and Q-band ESR, pulsed ESR, and UV-visible spectroscopies." *Journal of the American Chemical Society* 116 (14):6344-6353.
- Gunnlaugsson, Einar, and Asbjörn Einarsson. 1989. "Magnesium-silicate scaling in mixture of geothermal water and deaerated fresh water in a district heating system." *Geothermics* 18 (1-2):113-120.
- Haddad, Paul R, and Peter E Jackson. 1990. *Ion chromatography*. Vol. 46: Elsevier.
- Harris, Robin Kingsley. 1986. "Nuclear magnetic resonance spectroscopy."
- <http://xpssimplified.com/elements/calcium.php>. 28.01.2017.
- <http://xpssimplified.com/elements/magnesium.php>. 28.01.2017.
- Icopini, Gary A, Susan L Brantley, and Peter J Heaney. 2005. "Kinetics of silica oligomerization and nanocolloid formation as a function of pH and ionic strength at 25 C." *Geochimica et Cosmochimica Acta* 69 (2):293-303.
- Jensen, David S, Supriya S Kanyal, Nitesh Madaan, Michael A Vail, Andrew E Dadson, Mark H Engelhard, and Matthew R Linford. 2013. "Silicon (100)/SiO<sub>2</sub> by XPS." *Surface Science Spectra* 20 (1):36-42.
- Ketsetzi, Antonia, Aggeliki Stathoulopoulou, and Konstantinos D Demadis. 2008. "Being "green" in chemical water treatment technologies: issues, challenges and developments." *Desalination* 223 (1):487-493.
- Kim, Mi-Young, Ki Won Lee, Jung-Hyun Park, Chae-Ho Shin, Jaeyoung Lee, and Gon Seo. 2010. "Catalytic decomposition of nitrous oxide over Fe-BEA zeolites: Essential components of iron active sites." *Korean journal of chemical engineering* 27 (1):76-82.
- Kristmannsdóttir, Hrefna. 1989. "Types of scaling occurring by geothermal utilization in Iceland." *Geothermics* 18 (1-2):183-190.

- Kristmannsdóttir, Hrefna, Magnús Ólafsson, and Sverrir Thórhallsson. 1989. "Magnesium silicate scaling in district heating systems in Iceland." *Geothermics* 18 (1-2):191-198.
- Macarie, Lavinia, and Gheorghe Ilia. 2010. "Poly (vinylphosphonic acid) and its derivatives." *Progress in Polymer Science* 35 (8):1078-1092.
- Madejová, J. 2003. "FTIR techniques in clay mineral studies." *Vibrational spectroscopy* 31 (1):1-10.
- Matijević, Egon, and Dan Goia. 2007. "Formation mechanisms of uniform colloid particles." *Croatica Chemica Acta* 80 (3-4):485-491.
- Mekki, A, D Holland, CF McConville, and M Salim. 1996. "An XPS study of iron sodium silicate glass surfaces." *Journal of non-crystalline solids* 208 (3):267-276.
- Muralidhara, RS, CR Kesavulu, JL Rao, RV Anavekar, and RPS Chakradhar. 2010. "EPR and optical absorption studies of Fe 3+ ions in sodium borophosphate glasses." *Journal of Physics and Chemistry of Solids* 71 (12):1651-1655.
- Okayasu, Teruyuki, Kei Saito, Hiroyuki Nishide, and Milton TW Hearn. 2009. "Preparation of a novel poly (vinylsulfonic acid)-grafted solid phase acid catalyst and its use in esterification reactions." *Chemical Communications* (31):4708-4710.
- Palencia, Manuel, Bernabé L Rivas, and Eduardo Pereira. 2009. "Metal ion recovery by polymer-enhanced ultrafiltration using poly (vinyl sulfonic acid): Fouling description and membrane–metal ion interaction." *Journal of Membrane Science* 345 (1):191-200.
- Rivas, Bernabé L, Eduardo Pereira, Paola Gallegos, Daniela Homper, and Kurt E Geckeler. 2004. "Metal ion binding capability of the water-soluble poly (vinyl phosphonic acid) for mono-, di-, and trivalent cations." *Journal of applied polymer science* 92 (5):2917-2922.
- Saishu, Hanae, Atsushi Okamoto, and Noriyoshi Tsuchiya. 2013. "The Effect of Al and Na on the Precipitation Rate of Silica Minerals: Hydrothermal Flow-Through Experiments at 430° C and 31MPa." *Procedia Earth and Planetary Science* 7:762-765.
- Sjöberg, Staffan. 1996. "Silica in aqueous environments." *Journal of Non-Crystalline Solids* 196:51-57.
- Srinivasulu, K, I Omkaram, H Obeid, A Suresh Kumar, and JL Rao. 2013. "Use of Fe 3+ ion probe to study the structural coordination in sodium–lead borophosphate glasses by utilizing electron paramagnetic resonance and optical spectroscopy." *Journal of Alloys and Compounds* 546:208-215.

- Stáhl, Gabriella, György Pátzay, László Weiser, and Erika Kálmán. 2000. "Study of calcite scaling and corrosion processes in geothermal systems." *Geothermics* 29 (1):105-119.
- Swapp, Susan. 2012. "Scanning electron microscopy (sem)." *Geochemical Instrumentation and Analysis*.
- Tomaszewska, Emilia, Katarzyna Soliwoda, Kinga Kadziola, Beata Tkacz-Szczesna, Grzegorz Celichowski, Michał Cichomski, Witold Szmaja, and Jarosław Grobelny. 2013. "Detection limits of DLS and UV-Vis spectroscopy in characterization of polydisperse nanoparticles colloids." *Journal of Nanomaterials* 2013:60.
- Topcu, Gökhan, Aslı Çelik, Alper Baba, and Mustafa M Demir. 2017. "Design of polymeric antiscalants based on functional vinyl monomers for (Fe, Mg) silicates." *Energy & Fuels*.
- Weckhuysen, Bert M, Ralf Heidler, and Robert A Schoonheydt. 2004. "Electron spin resonance spectroscopy." In *Characterization I*, 295-335. Springer.
- WES JEC. 2006. "Report on Geothermal Development Survey in the Canakkale-Tuzla Field. West Japan Engineering Consultants, Inc., Turkey.".
- Whittig, LD, and WR Allardice. 1986. "X-ray diffraction techniques." *Methods of Soil Analysis: Part 1—Physical and Mineralogical Methods* (methodsofsoilan1):331-362.
- Wolf, RE. 2005. "What is ICP-MS? and more importantly, what can it do." *US Geological Survey* 7.
- Yamashita, Toru, and Peter Hayes. 2008. "Analysis of XPS spectra of Fe 2+ and Fe 3+ ions in oxide materials." *Applied Surface Science* 254 (8):2441-2449.
- Zhang, Bing-Ru, Yu-Ning Chen, and Feng-Ting Li. 2011. "Inhibitory effects of poly (adipic acid/amine-terminated polyether D230/diethylenetriamine) on colloidal silica formation." *Colloids and Surfaces A: Physicochemical and Engineering Aspects* 385 (1):11-19.
- Zhang, Shouwei, Wenqing Xu, Meiyi Zeng, Jie Li, Jiaxing Li, Jinzhang Xu, and Xiangke Wang. 2013. "Superior adsorption capacity of hierarchical iron oxide@magnesium silicate magnetic nanorods for fast removal of organic pollutants from aqueous solution." *Journal of Materials Chemistry A* 1 (38):11691-11697.